2022-12-01

High-Temperature Valve Design For A Solid Oxide Fuel Cell/gas Turbine Hybrid System Utilizing Smart Materials

Alba Jazmin Leyva
University of Texas at El Paso

HIGH-TEMPERATURE VALVE DESIGN FOR A SOLID OXIDE FUEL CELL/GAS TURBINE HYBRID SYSTEM UTILIZING SMART MATERIALS

ALBA JAZMIN LEYVA MARQUEZ

Doctoral Program in Mechanical Engineering

APPROVED:

Yirong Lin, Ph.D., Chair

Bill Tseng, Ph.D., Co-Chair

Angel Flores, Ph.D.

Joel Quintana, Ph.D.

Stephen L. Crites, Jr., Ph.D.
Dean of the Graduate School

Dedication

This work is dedicated to my family, friends, and teammates who have been with me since the start of this academic adventure.

HIGH-TEMPERATURE VALVE DESIGN FOR A SOLID OXIDE FUEL CELL/GAS TURBINE HYBRID SYSTEM UTILIZING SMART MATERIALS

by

ALBA JAZMIN LEYVA MARQUEZ, B.S.M.E., M.S.M.E.

DISSERTATION

Presented to the Faculty of the Graduate School of

The University of Texas at El Paso

in Partial Fulfillment

of the Requirements

for the Degree of

DOCTOR OF PHILOSOPHY

Aerospace and Mechanical Engineering

THE UNIVERSITY OF TEXAS AT EL PASO

December 2022

Acknowledgments

This project was done and finished thanks to the support and mentorship of my advisor, Dr. Yirong Lin, without him taking the project from a previous faculty member in the Department of Mechanical Engineering, this project would not be able to be completed. Thanks to the Department of Energy for their interest and sponsorship of the project. I would also like to thank the team that lead the project before me and my recent teammates, Ariztbe Valladolid, Nicolas Herrera, Saqlain Zaman, Sahid Hassan, and Sergio Sepulveda, without them the project will not be what it is today.

I would like to thank my family and friends for all their support throughout this journey. Finally, I want to especially thank Dr. Bill Tseng, Dr. Angel Flores, and Dr. Joel Quintana for being part of my committee and for their time and interest in this project.

Abstract

The topic of this project includes extensive research on the Solid Oxide Fuel Cell Gas Turbine (SOFC/GT) hybrid system located at the National Energy Technology Laboratory. The goal is to reduce pollution and generate energy by using natural gas and a combination of fuel cells, heat exchangers, bypass valves, turbines, and combustors as components working together to produce clean energy. The SOFC/GT system works by having the fuel cell pressurized by the gas turbine. The turbine then produces exhaust gas for the fuel cell, because the turbine recovers the majority of the heat and the pressurization contributes to the enhancement of fuel cell characteristics, this system is regarded as efficient. A bypass valve design is proposed to further enhance this system's efficiency, despite its effectiveness.

This project aims to develop and manufacture a functioning bypass valve that will be incorporated into the SOFC/GT system to regulate gas turbine exhaust airflow. The system's efficiency is expected to rise as a result of this action. Smart materials, Shape Memory Alloys (SMA), were used to create a new valve that was available at a price that was more reasonable because, regrettably, this valve is not manufactured at a low cost in the market. The design aims to modify this new material for testing and collecting data.

The project starts focusing on creating and designing a valve prototype for room temperature testing. Data was gathered by doing several trial tests before jumping into the design and manufacture of the high-temperature bypass valve. Once the room-temperature prototypes proved their functionality in controlling airflow and using SMA springs for actuation, the design for the high-temperature bypass valve was created and manufactured for laboratory testing before installation at the SOFC/GT system.

Table of Contents

List of Tables

List of Figures

List of Graphs

SECTION 1: VALVE DESIGN FOR A SOFC/GT HYBRID SYSTEM UTILIZING SMART MATERIALS

Chapter 1: Background and Introduction

The study proposes a high-temperature, and pressure bypass valve to control the airflow going towards a turbine and heat exchanger during the startup of a Solid Oxide Fuel Cell/Gas Turbine (SOFC/GT) hybrid system.[1], [2] To control the high temperatures that are exhausted from the post-combustor, the bypass valve will be placed before the heat exchanger to regulate the airflow going to the fuel cell and avoid thermal stress on the material. The valve must remain partially open to maintain a certain amount of heat flowing through to keep the system operating during startup, where the turbine must also reach a nominal speed of 40,500 rpm. This project's primary goals are to design, manufacture, and test a bypass valve able to endure high temperatures and pressure airflow during the start of a cyber-physical SOFC/GT hybrid system.

Smart material actuators are made of materials that can change shape and respond to changes in the environment. The function of these devices is to generate the necessary force to move another mechanical device. Piezoelectric materials [3], magnetostrictive materials [4], and shape memory alloys are the three main secular groups utilized as smart material actuators. A change in shape caused by electric, electromagnetic, or thermal stimulation is what gives them the ability to act.[5] The use of shape memory alloy to actuate valves has several advantages. It is less expensive than other systems. Additionally, the absence of a mechanical gearbox or motor makes the valve lighter. Shape Memory Alloy (SMA) springs were tested on the valve actuation, resulting in a good relationship between time and position when opening and closing the valve.

1.1 Department of Energy Hyper Facility

The SOFC/GT hybrid system can be found in the United States Department of Energy's National Energy Technology Laboratory (NETL) located in Morgantown, West Virginia. Figure 1 represents the concept behind the SOFC/GT system. The SOFC/GT hybrid system operates at high temperatures of up to 1100°C to 1200°C. However, in the precise area where the valve is intended to be used, temperatures can range from 250°C to 650°C at 1 atm pressure. The orange circle in the figure represents the position where the bypass will be installed.

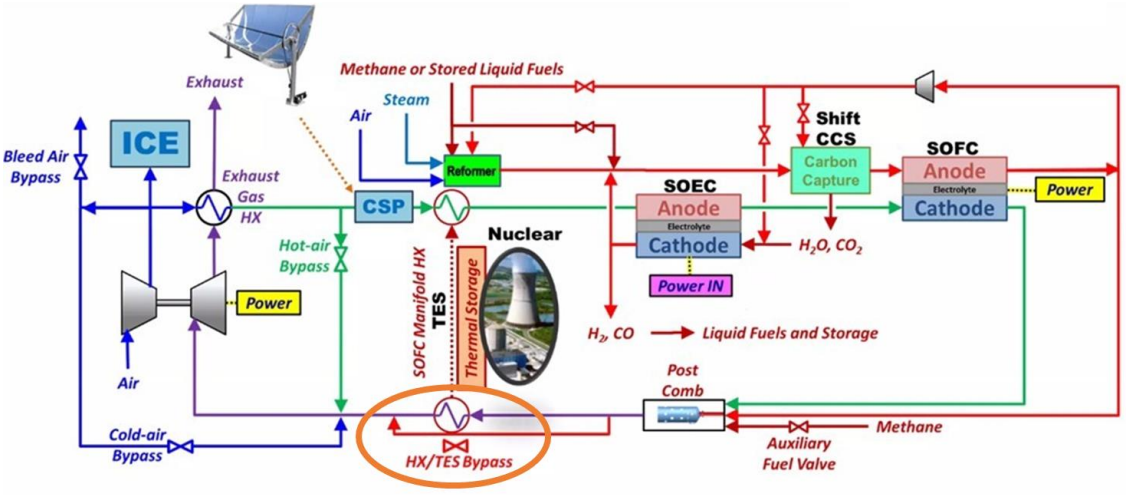

Figure 1: SOFC/GT Hybrid Performance Project Diagram

Due to the high level of complexity required for a design that can withstand extremely high temperatures, high-temperature valves are difficult to find on the market. A custom design is possible for many laboratories or businesses, but it can be costly. Since this research area has the potential to become very efficient for a hybrid system, the objective of NETL is to open new development avenues in this area. In addition to saving money, new development concepts for this study enable researchers to investigate a variety of valves and broaden their knowledge for new applications. Numerous piping valves were studied to discover various market-available designs.[6], [7]

1.2 Design Background

It was necessary to produce the designed valve and test it in a laboratory setting, before jumping into the high-temperature design, in order to demonstrate that it was appropriate to control or manipulate the flow through any pipe. As a result, Additive Manufacturing (AM) was chosen as the most preferred manufacturing technique for laboratory testing. AM is the process of combining through fusion, binding, or solidification, such as powders and liquid resins. Using 3D CAD modeling, it builds the part layer by layer.[8], [9] AM technologies have developed in a variety of ways. Fused deposition modeling (FDM) [10] and selective laser sintering (SLS) [11] are utilized for thermoplastic and thermoset polymer printing; for ceramic printing direct ink write (DIW) [12] is used; powder bed fusion [13], directed energy deposition (DED) [14], and binder jetting [15] are used for metal 3D printing; Stereolithography (SLA) [16] can be used to create photopolymer resin prototypes or models. SLA was the ideal material for making the prototype valve for this study. The SLA technique was chosen because it's easy to print and modify, provides precise final resolution, and is less expensive.

There is one major drawback to using SMA springs for valve actuation, despite their numerous advantages. These springs don't do much to exert force. To solve this issue, the valve's disc was hollowed out from the back to reduce the amount of weight needed to be actuated, and the rod where the springs would be connected was made a little longer so that the spring could generate sufficient torque. Additionally, an O-ring was used to seal the top side of the valve to prevent any friction with the body. The SMA mounting location is raised above the valve's center, centering the design of the valve on a solid piece construction. Two integrated stoppers and pass-through holes in the SMA mounting box prevent the rod from being oversized. Additionally, the additional connection points for the power supply were made possible by the pass-through holes,

which made assembly easier. To allow the rod to pass through the center, the plate was tapered toward the edge. The individual pieces would be held together with screws or bolts.

A bypass valve that would be operated by SMA springs was designed and tested in this project. The valve was 3D printed using photo-resin using the SLA printing method to confirm the design's efficacy. Furthermore, the valve was actuated with shape memory alloy springs, and the actuation rate was determined by varying electrical inputs. It has been demonstrated that using SMA for quick response actuation to control the valve is possible. In addition, it is essential to emphasize that the design proved to be suitable for high-temperature operations as well, requiring only the conversion of the valve material into high-temperature sustaining materials.

1.3 Shape Memory Alloys

Shape memory alloys (SMAs) have received a lot of attention lately due to the fact that they are smart materials and functional materials. SMAs are metals capable of recuperating a predetermined shape just while reaching up to a crucial transformation temperature.[17] They are based on a specific martensitic transformation (thermoelastic) that takes place in various metallic alloys.[18] The list consists of Nickel Titanium (NiTi), copper/Aluminum/Nickel (CuAlNi), Copper/Zinc/Aluminium (CuZnAl), Gold/Cadmium (AuCd), among many more metals.[19] The most commonly used SMA is NiTi, where the shape recovery is triggered by temperature and stress.[20] When subjected to applied mechanical cyclic loading, SMAs undergo a reversible hysteretic shape change, allowing them to absorb and release mechanical energy. SMAs are well-suited for applications involving sensing and actuation, impact absorption, and vibration damping due to their distinctive properties; making them perfect to be used in a variety of industrial sectors such as aerospace, automotive, biomedical, and oil exploration.[21]

Because the alloys can regain their shape when heated, they are referred to as shape memory alloys. To put it another way, the material is put under stress, which causes it to deform. Heat is applied to the material, which will restore its original shape. Two types of memory effects exist: one-way, which recalls memories at a single temperature, and two-way, which recalls memories at two distinct temperatures. The shape memory alloy's thermal behavior is divided into two phases: austenite (heating), which begins at As and ends at Af, and martensite (cooling), which begins at Ms and ends at Mf. With each thermal cycle, the graph of the thermal behavior changes, increasing the likelihood of hysteresis.[22], [23]

Additionally, this material is very useful because it can be trained to move in particular directions. To put it another way, depending on the requirements of the project, it can generate more or less movement if the appropriate training procedure is followed. The two-way shape memory composite's preparation requires a thermo-mechanical cycle or treatment before it can show the consequences of preparation. In order to accomplish this, specific angles are selected for both high and low temperatures, and then they are placed in high temperatures to maintain their high-temperature shape and in low temperatures to maintain their low temperature shape. After that, the material will maintain its high-temperature shape during heat waves and its cold temperature shape during cooling. The same procedure is followed for an alloy with one-way shape memory. Use thermal cycling, which maintains a constant temperature above Af without placing any stress on the material in the position you want it to remember.[24]–[26]

1.4 OBJECTIVE

The goal is to create, design, and manufacture a low-cost valve for the Solid Oxide Fuel Cell/Gas Turbine hybrid system at NETL by using smart materials as actuators. The bypass valve

needs to withstand a temperature of 650°C and be actuated utilizing the selected smart material for the job, shape memory alloy springs. The tasks expected to achieve this objective are listed below:

1. Design and manufacture a valve prototype to test at a room temperature environment.
2. Test and analyze the shape memory alloy springs to determine the actuation development.
3. Install shape memory alloy springs into the design to test out their capacity to actuate the valve and control the airflow of 60 L/min.
4. Finalize prototype, record results, and move on to high-temperature design.
5. Modify design for a high-temperature environment.
6. Test and analyze shape memory springs on the final manufactured high-temperature design.
7. Ship bypass valve to NETL for installation.

Chapter 2: Theory

The theory underlying the computations for a shape memory alloy spring is explained in this chapter. The calculations below can serve as a guide for creating the prototype. It's critical to realize that the majority of the equations presented in this chapter can be used to kick off the design of a SMA spring. The equations here provided help in determining the spring parameters useful for this project.

2.1 Shape Memory Alloys Calculation Theory

The internal phase of transformation in shape memory alloys is responsible for their nonlinear behavior. The mechanism by which the crystalline structure changes from one form to another is produced by this transition. Martensite (low-temperature phase) and austenite are two unique phases that these smart materials go through (high-temperature phase). Shape memory springs are subjected to many stages of actuation, and each phase has two different temperature values that describe these stages. The start and end transformations for each phase are determined by these four temperatures, as shown in figure 2. [27], [28] SMA temperature hysteresis between the austenite phase and the martensite state is one thing to take note of because it demonstrates that the transformation from austenite to martensite won't be the same or exact.

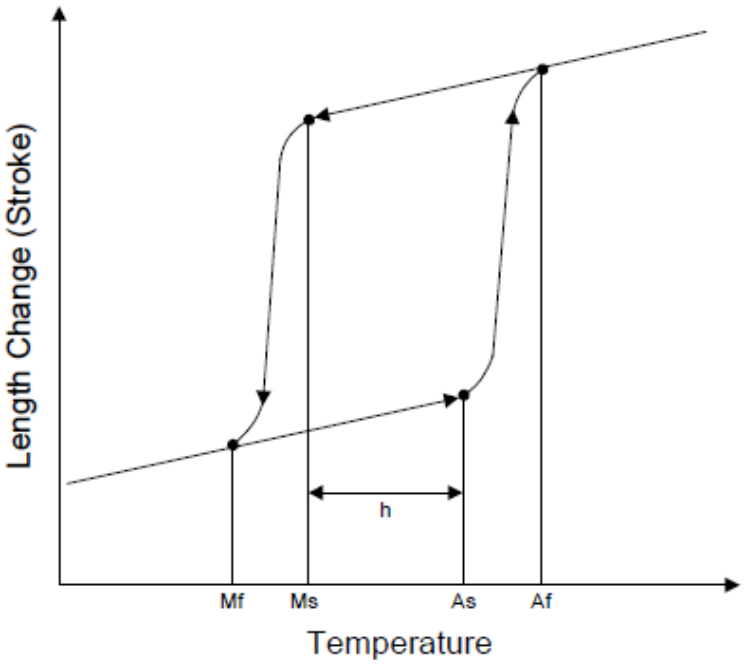

Figure 2: SMA Length vs Temperature[27]

Table 1: Characteristic Temperatures of SMAs

Ms	Martensite start temperature upon cooling
Mf	Martensite finish temperature upon cooling
As	Reverse transformation starts temperature upon heating
Af	Reverse transformation finish temperature upon cooling

The spring's force is linearly proportional to its material's shear modulus at any given deflection.[29] The expression for shear stress and strain relation in an SMA spring is described as the following,

$$\tau - \tau_o = G(\gamma - \gamma_o) + \frac{\Omega}{\sqrt{3}}(\xi - \xi_o) + \frac{\Theta}{\sqrt{3}}(T - T_o) \qquad \text{(Shear Stress, Strain Relation)}$$

$$\Omega = -D\varepsilon_L \qquad \text{(Phase Transformation Tensor)}$$

$$\xi = \Xi(\sigma_{eq}, T) \qquad \text{(Variable, Degree of Martensitic Transformation)}$$

Where G is the elastic shear modulus, τ is the shear stress, γ is the strain, Ω is the phase transformation tensor, Θ is the thermoelastic tensor related to the thermal expansion of the SMA material, T is the temperature, and ξ is the internal variable describing the degree or martensitic transformation.[30]

Table 2: Properties of Nitinol Used in Calculations[31]

$\frac{MPa}{°C}$			GPa		°C					
C_M	C_A	Θ	D_M	D_A	M_f	M_s	A_s	A_f	$\varepsilon_L(\%)$	n
10.3	10.3	0.55	26.3	67	9	18.4	34.5	49	6.7	0.85

2.1.1 Total Deflection Calculations

To calculate the total deflection of the shape memory alloy springs during actuation, the formulas used are those of regular springs with their specific characteristics.

$$\tau_{max} = K\frac{2FR}{\pi r^2} \quad \text{(Spring max shear)}$$

$$\gamma = \frac{\tau}{G} = \frac{2FR}{\pi r^3 G} \quad \text{(Hooke's Law of Torsion)}$$

$$\alpha = \int_0^{2\tau RN} \frac{\gamma}{r} dx = \frac{4FR^2N}{r^4G} \quad \text{(Angular Deflection)}$$

$$y = \alpha R = \frac{4FR^3N}{r^4G} \quad \text{(Total Deflection)}$$

Where K is the Wahl correction factor, it's related to the change in the coil of the spring, F is the external force created by the spring, R is the mean radius of the spring, r is the radius of the spring's wire, N is the total number of coils of the springs, and as stated before is the shear modulus. The shape memory alloy spring material used for this research is Nitinol (Nickel-Titanium). This material was chosen due to previous studies made on NiTi alloys showing better corrosion resistance, biocompatibility, high deformation recovery, and higher electrical resistance for resistive heating in actuator applications.[32]

Table 3: Properties of Nitinol SMA Springs Obtained from Supplier

Wire size	Mandrel Size	Pitch	Transition temperature
1mm	8mm	1mm	80℃

2.1.2 Spring Load Capacity Test

The ability of each spring to produce a certain amount of force was crucial in determining whether the SMA spring could trigger the valve. To check that, initially, the spring was stretched from an initial length of 13mm to a length of 42.5mm. Then one end of the spring was fixed with a clamp, and the other was hooked with a fish weighing scale which was also fixed and tared to zero (Figure 3). Then DC electrical power was supplied, connecting positive and negative lines at both ends of the SMA spring to the power supply. The values are shown on the scale in kilograms with the spring compression. Later it was converted into newton(force).

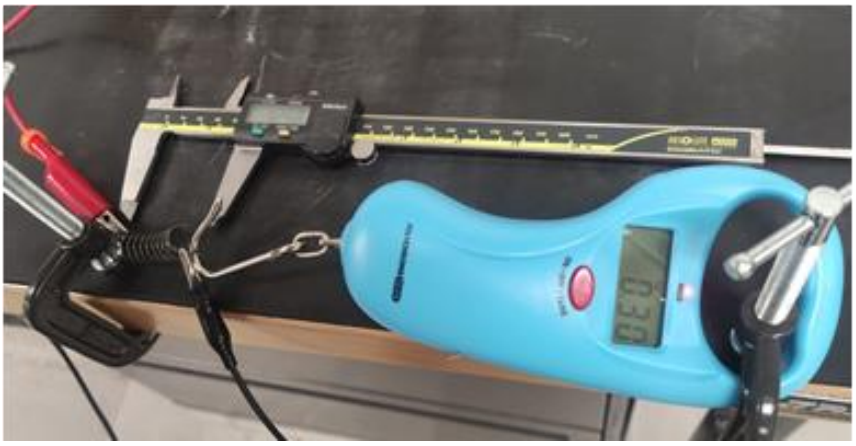

Figure 3: Setup for SMA Spring Load Capacity Test

Chapter 3: Design Model for Room Temperature Testing

To be able to successfully create a working high-temperature valve from scratch, several commercial valves were studied to understand their workability that best applies towards our expected design. The commercial valve that was used to kind of recreate their mechanism is the butterfly valve. This valve was chosen because in its design you see it uses a disk to regulate the flow, and the disk is controlled outside of the flow by a torsion movement.[33] The design mimics the movement of a butterfly valve, except for using smart materials to facilitate and simplify the movement, with some improvements in flow control and automatic actuation. Manufacturing the designed valve and testing it in a lab environment was necessary to show that the valve model was suitable to regulate or control the flow through any pipe.

3.1 Design Constraints

When dealing with the aspects required for any design project, one must consider the scope, time, cost, and quality. When testing, time is crucial, important tasks to complete in conjunction with a timeline include ordering supplies, creating prototypes, and testing the prototypes. The budget is a crucial consideration when creating a high-quality project. To guarantee a durable valve prototype, selecting parts and adjusting were all considered in the manufacturing of a lifetime product. In the case of this project to help stay inside the budget, a prototype made of PVC pipes was created due to the fact that is an inexpensive material and it's easy to work with. The budget also needed to be taken into account when selecting a dependable actuator, which is why SMA springs were chosen for the job, apart from being economically advantageous, their mechanical properties met the requirements for the project. To be able to also have more accessibility to pieces and to make modifications more easily, the designed valve for room temperature is a 3D printed prototype valve made with photopolymer resin stereolithography (SLA). SLA method was

selected because it's easier to print, and modify, provides precise final resolution, and is less expensive.

3.2 Boundary Conditions

Since the SOFC/GT system exhaust turbine space may only be modified to certain parameters, the valve's design must adhere to specific dimensions that cannot be exceeded, such as a height of 5 inches. With the use of shape memory alloys, the valve should be capable of being completely open and completely closed while controlling at least 80% of the flow. To mimic the fluxes of the SOFC/GT system, this flow must be subjected from 60 L/min to 80 L/min. The goal of the study is to demonstrate that the shape memory alloy springs can function as valve actuators at room temperature testing to later on make changes to prove their workability in high-temperature environments.

Table 4: Room Temperature Lab Prototype Boundary Conditions

Fluid	Air
Volumetric Flow Rate	60 L/min – 80 L/min
Temperature	25˚C
Pipe Material	PVC
Valve Material	Ceramic Resin

3.3 Design Approach

The valve design is a crucial part of the project, and five factors were considered to achieve the project goal.

Table 5: Factors Considered for Design

1. Airflow re-direction
2. Shape memory alloy placement for actuation

3. Light rotating parts
4. Leakproof
5. Shape memory alloys springs wiring

3.3.1 First Design Iteration

The first design as seen in figure 4 is nothing compared to the butterfly valve. This is because before settling into mimicking the butterfly valve. The team tested a different approach to achieve the requirements needed. On figure 4 and figure 5 one can notice that it only is half a pipe where this will be mounted on the pipe to control the flow. The rod and disc tested with this design were made of stainless steel, the rod will go through the hole in the design, and after that the disc will be attached to the rod with screws. The advantages of this design included cost effectiveness because less material was needed to work with and convenient accessibility for installing the shape memory alloy springs at the top of the design.

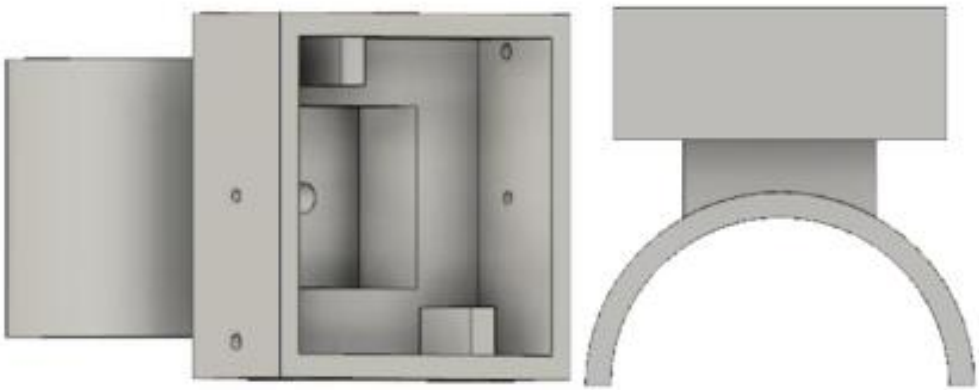

Figure 4: CAD Design of First Design Iteration

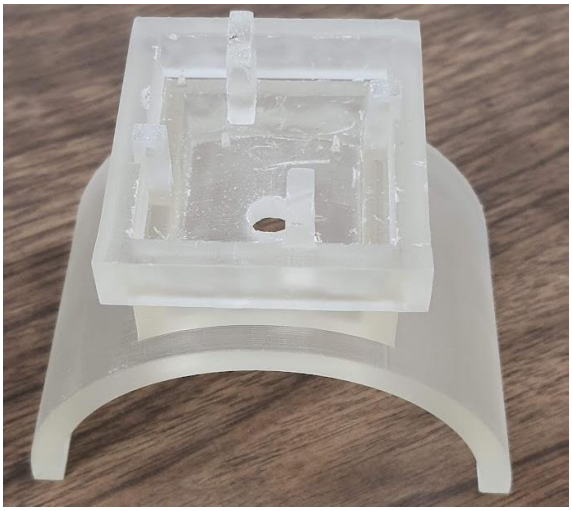

Figure 5: 3D Printed Clear Resin Design

Figure 6: Testing of First Prototype

The main issue when operating the experimental setup, as seen in figure 6, are air gaps and small cavities resulting in leakages throughout the system, mainly on the top part of the design. To be able to get good airflow results for this design, the valve needed to be completed seal all around the sides and top of the design.

Figure 7 illustrates the prototype's airflow direction, for this design and the following designs. It is possible that leaks may occur through the mount as a result of the increased pressure created by the valve when it closes. To adjust the mass flow rate and ascertain how much flow the

valve can manage, the prototype was built with one inlet and two outlets. For the testing of the valve mount, it was connected to a 3inch PVC pipe on both ends, with a Y-type connection.

Table 6 demonstrates the results of the first tests with an inlet of 20 L/min. Flow meters were placed on the inlet and each outlet to measure the actual flow and how much can the valve redirect the flow. The leakage found in the valve is minimal as observed, demonstrating the airflow control. As the table shows that approximately 90% of the airflow in the system is conserved and 10% is lost due to leakages.

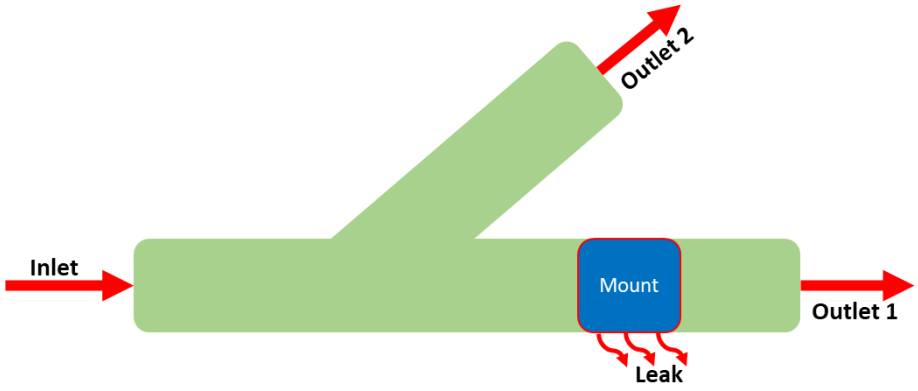

Figure 7: Flow Direction Schematic

Table 6: Airflow Results of First Design Iteration

		L/min			
Test Run	Valve	Inlet	Outlet 1	Outlet 2	Leak
1	Open	20	9	10	1
	Closed		10	10	0
2	Open	20	11	9	0
	Closed		10	10	0
3	Open	20	9	9	2
	Closed		8	9	3
4	Open	20	11	9	0
	Closed		10	10	0
5	Open	20	10	10	0
	Closed		10	10	0

3.3.2 Second Design Iteration

For the second design iteration, the team jumped up to work on mimicking the work method of a butterfly valve. As seen in figure 8, this design consists of having two sides that are attached together by nuts and bolts. The benefits of this design are that it had more flow control, and it was easier to work with if any changes are needed. To prevent the drawback of having leaks on the top of the mount design and on the sides, sealant was used as a gasket on the sides of the design to achieve better airflow results.

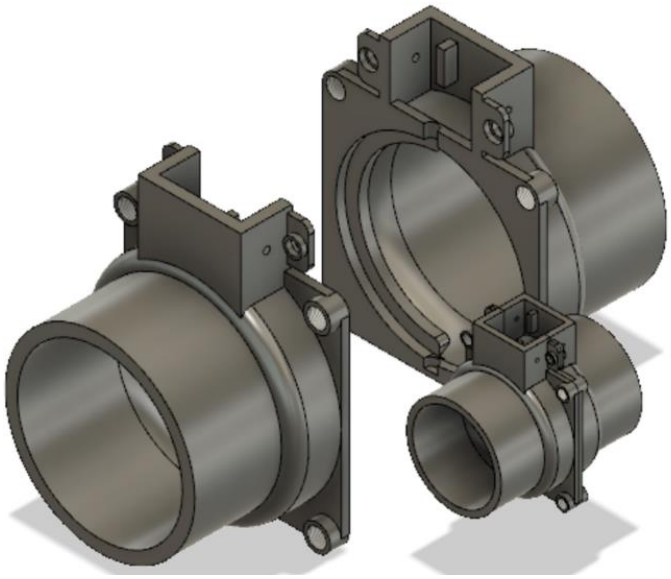

Figure 8: CAD Design of Second Prototype

Figure 9: Testing of Second Prototype

After sealing the valve completely as shown in figure 9, table 7 shows that approximately 65.80% to 86.7% of the airflow in the system is conserved and 13.3% to 34.2 is lost due to leakages. The sealing method used was butyl tape and O-rings.

Table 7: Airflow Results of Second Design Iteration

		L/min			
Test Run	Valve	Inlet	Outlet 1	Outlet 2	Leak
1	Open	60	22	22	16
	Closed		22	22	16
2	Open	60	21	22	17
	Closed		21	22	17
3	Open	60	22	21	17
	Closed		22	22	16
4	Open	60	23	22	15
	Closed		24	24	12
5	Open	60	25	24	11
	Closed		25	25	10
6	Open	60	26	26	8
	Closed		26	26	8

3.3.3 Third Design Iteration

Looking at the previous design iteration and the airflow results taken, it is shown that the approach of mimicking a butterfly valve is the way to go to achieve all our requirements to have a

successful working valve. With this we jump into the third design iteration, figure 9 shows that the design changed a little from the one before. The new design offers instead of being two separate parts, now it is a whole single part for the mount. The disc will be placed inside the mount by one side while the rod slides down by the hole on top of the mount.

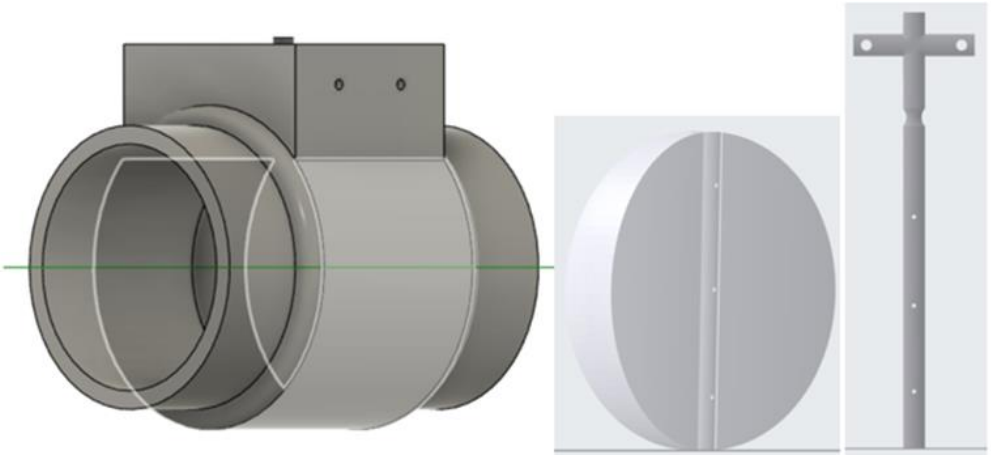

Figure 9: CAD Design of Third Prototype

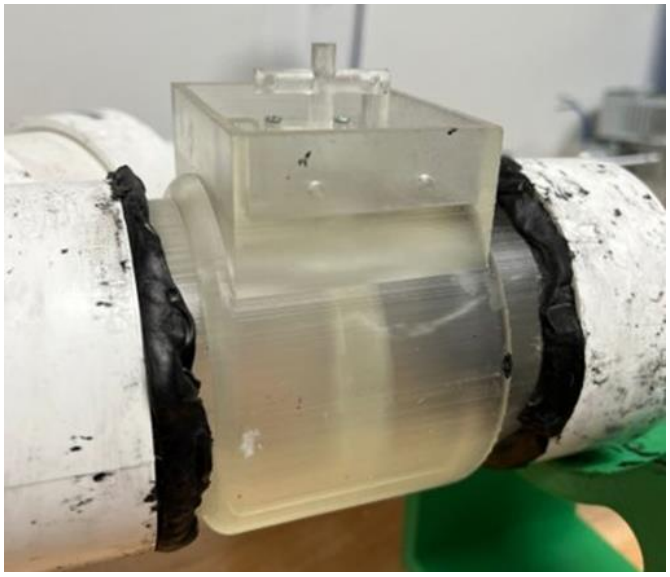

Figure 10: 3D Printed Clear Resin Design

Figure 11: Testing of Third Prototype

The benefits of this design are that know there are no leaks coming from the design. To achieve this the team considered more aspects of the butterfly valve mechanism than the previous iteration. After securely installing the valve in the laboratory prototype as shown in figure 11, table 8 shows that approximately 88.3% to 95% of the airflow in the system is conserved and 4.9% to 13.3% is lost throughout the system. The sealing method used was butyl tape and O-rings.

Table 8: Airflow Results for Third Design Iteration

		L/min			
Test Run	Valve	Inlet	Outlet 1	Outlet 2	Leak
1	Open	60	28	26	6
	Closed		26	26	8
2	Open	60	28	26	6
	Closed		29	28	3
3	Open	60	28	28	4
	Closed		26	27	7
4	Open	60	27	26	7
	Closed		26	26	8
5	Open	60	29	26	5
	Closed		26	29	5

3.4 Safety Analysis

The ability to prevent leaks made the final design iteration the best option for laboratory testing conditions. This made it possible to reduce risks and control airflow for more effective results. This implies that the system's lifespan will lengthen.

The top portion of the design was created to protect the shape memory alloy springs from the direct flow. This method makes it simpler to install the springs and set up the cooling system to maintain them at room temperature, ensuring that the springs will only be acting when activated and not respond to changes in external temperatures. Insulating the cables that will link the power source and the SMA springs is another technique to reduce dangers. By doing so, we can prevent issues caused by a short circuit or even an accident. All necessary safety precautions were taken within the lab, including wearing the appropriate attire, gloves to prevent any electrical accidents, eye safety goggles, etc.

3.5 SMA Actuation Results

Before testing the valve with the shape memory alloy springs installed on the mount. The workability of the springs had to be tested on their own. Therefore, relationships of voltage, current, and time were done for when the spring is enlarged to 42.87 mm and how it compresses back to its original length which is 13.05 mm, as seen in the next tables and graphs. A DC power supply was applied, connecting the positive and negative wires at the SMA spring's two ends to the power source. In the spring, this electrical source produces heat, which after this the spring starts to contract and get back to its former size. It was noticed how long it took for the springs to compress to their initial shape.

Table 9: Constant Voltage but Variable Current on SMA springs

Set Voltage	Current	Time When Fully Contracted (min, sec)
5 V	1 amp	4:20
5 V	2 amp	0:22
5 V	3 amp	0:10
5 V	4 amp	0:06
5 V	5 amp	0:03

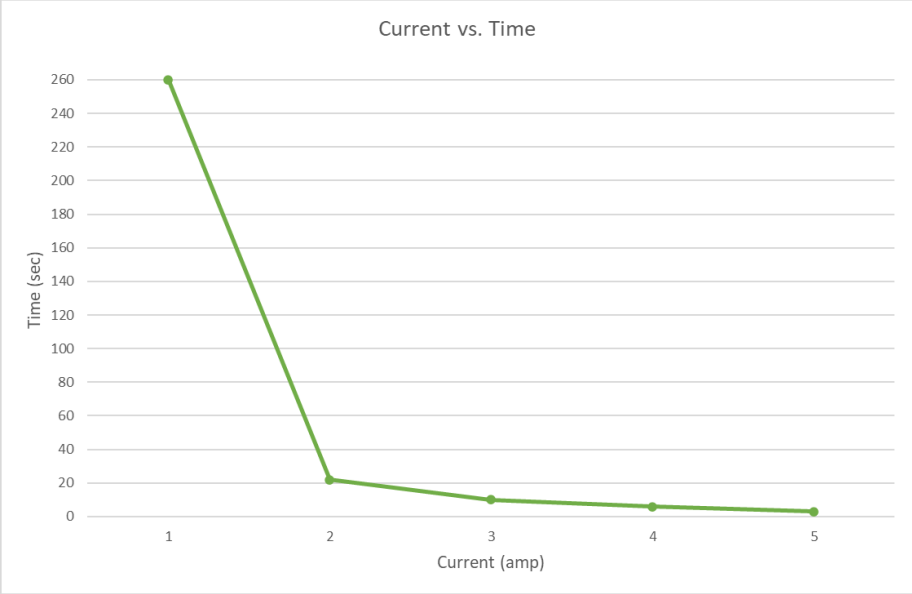

Graph 1: Variable Current vs. Time, For a Constant Voltage

Table 10: Constant Current with Variable Voltage on SMA springs

Voltage	Set Current	Time When Fully Contracted (min, sec)
1 V	3 amp	1:50
2 V	3 amp	0:17
3 V	3 amp	0:10
4 V	3 amp	0:09
5 V	3 amp	0:09

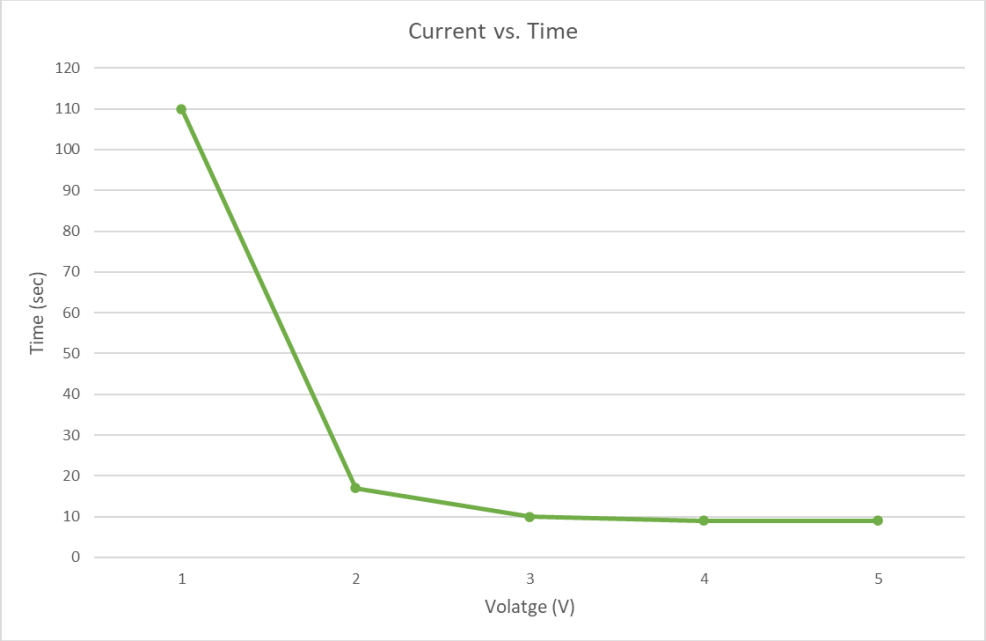

Graph 2: Variable Voltage vs. Time, For a Constant Current

After the initial testing, it was discovered that the voltage setup is actually the maximum voltage set up in the power supply, not the actual voltage that is actually applied to the springs. In another words, there are times when the spring will return to its initial length without reaching the maximum voltage set in the power supply. For this reason, additional testing was carried out

to determine the actual current and voltage at which the shape memory alloy spring is activated. The tables below demonstrate the various timings between voltage, current, and time actuation of the springs, with set max voltage and current.

Table 11: Maximum Voltage Set at 1V

Max Voltage	Max Current	Found Voltage	Found Current	Time (min, sec)
1 V	1 amp	.80	1.00	4:11
1 V	2 amp	1.00	1.24	1:20
1 V	3 amp	1.00	1.23	1:18
1 V	4 amp	1.00	1.25	1:14
1 V	5 amp	1.00	1.27	1:13

Table 12: Maximum Voltage Set at 2V

Max Voltage	Max Current	Found Voltage	Found Current	Time (min, sec)
2 V	1 amp	.78	1.00	4:19
2 V	2 amp	1.50	2.00	0:25
2 V	3 amp	2.00	3.00	0:14
2 V	4 amp	2.00	2.99	0:12
2 V	5 amp	2.00	3.00	0:11

Table 13: Maximum Voltage Set at 3V

Max Voltage	Max Current	Found Voltage	Found Current	Time (min, sec)
3 V	1 amp	.75	1.00	4:34
3 V	2 amp	1.55	2.00	0:23
3 V	3 amp	2.33	2.99	0:09
3 V	4 amp	2.71	4.00	0:05
3 V	5 amp	3.00	4.68	0:04

Table 14: Maximum Voltage Set at 4V

Max Voltage	Max Current	Found Voltage	Found Current	Time (min, sec)
4 V	1 amp	.74	0.99	4:36
4 V	2 amp	1.47	2.00	0:22
4 V	3 amp	1.88	3.00	0:10
4 V	4 amp	2.77	4.00	0:06
4 V	5 amp	3.30	5.00	0:03

Table 15: Maximum Voltage Set at 5V

Max Voltage	Max Current	Found Voltage	Found Current	Time (min, sec)
5 V	1 amp	.76	1.00	4:28
5 V	2 amp	1.49	2.00	0:22
5 V	3 amp	2.00	3.00	0:09
5 V	4 amp	2.69	4.00	0:05
5 V	5 amp	3.30	5.00	0:03

The graph below shows how these two variables, current and time of actuation, are inversely related. Less current denotes a longer actuation time, whereas higher current denotes a quicker actuation time.

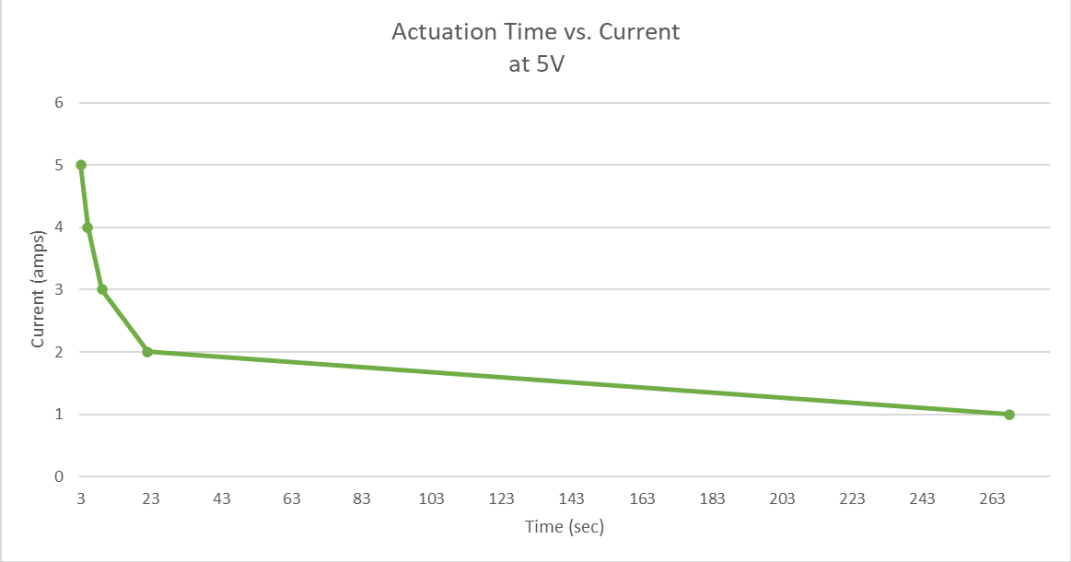

Graph 3: Actuation Time vs. Current, at 5 Volts

3.6 Conclusion

To prove that the designed valve works, three different iterations of the design were 3D printed using SLA technology and actuated with a SMA spring while redirecting a compressed air flow of 60 L/min at room temperature. The third design iteration proved to be the best in flow

control and actuation time. By making just one single print for the mount we manage to seal completely all leaks coming from the valve itself. SMA spring prove to operate in the third valve prototype, by achieving the fastest recorded actuation time which was around 3 seconds with 5 volts and 5 amps D.C electrical supply. By applying more current to the springs we can see a quicker response. Test results show that SMA springs can be explored in valve systems to control airflow during actuation.

3.6.1 Future Work and Recommendations

For future work by taking the results given by all the iterations, the designs can continue to be modified and upgraded to achieve flow control at greater flow rates. The material used for 3D printing the valve can be changed to compare the results to the ones calculated in this chapter. By playing around with different materials, the aspects and the characteristics of the prototypes can be upgraded and be used in different applications. Since the highest temperatures possible to work within the lab go from 80℃ to 98℃, the recommendation is to make the necessary updates on the designs to test at those temperatures and compare with room temperature results.

Chapter 4: Design Model for High-Temperature Testing

This chapter consists of what was tested in the previous chapter. The goal is to design and manufacture a bypass valve to control airflow in a SOFC/GT system. Considering the results from the room temperature test, moving on to the high-temperature design. The idea of mimicking the mechanism of a butterfly valve was still considered. The valve will be placed in the exhaust of the turbine going into the recuperator inlet. A 2-inch or 3-inch hole will be drilled into the bottom of that 8-inch pipe. The size of the hole will depend on the valve requirements. A cooling system is thought to be connected to the SMA chamber in order to prevent overheating the springs and compromising their workability. Figure 12 shows the location of the valve installation for the project.

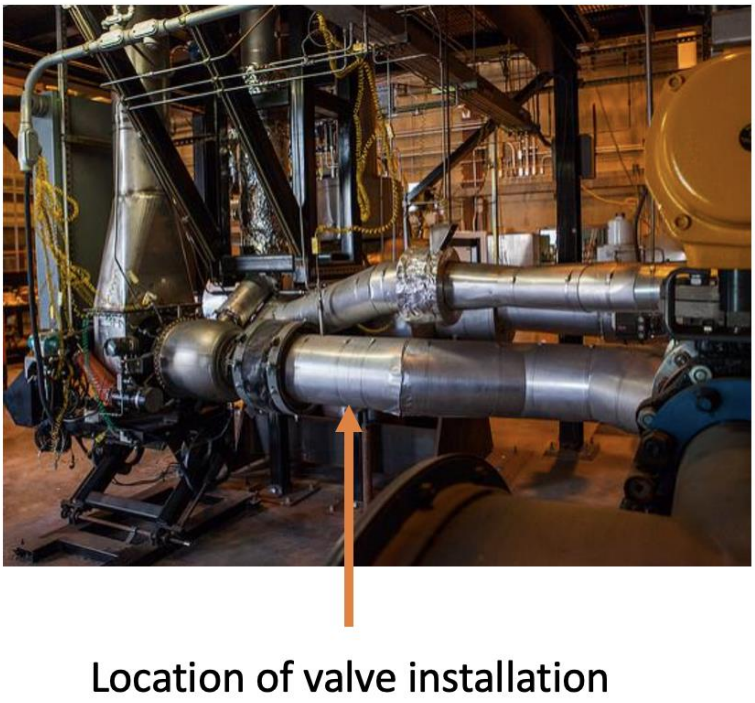

Figure 12: Location of the Valve in the Actual Hyper Facility courtesy of NETL

4.1 Design Constraints

With the help of the previous studies and their design constraints. The project moves to take into consideration the design constraints involving the manufacturing cost and material for a valve that is able to withstand high temperatures in the range of 600℃ - 1000℃. As stated, before when dealing with the aspects required for any design project, one must consider the scope, time, cost, and quality. For this chapter, the material changes to one that can be able to work in a high-temperature environment, easy to find, and easy to manufacture. Due to the results given with the SMA springs on the room temperature prototypes, they will be used to actuate the high-temperature design valve. This research aims to significantly reduce the cost and weight of traditional valve technology by developing a valve that uses smart materials in its operation.

4.2 Boundary Conditions

In the laboratory, the possible testing high temperatures vary between 80 ˚C - 98 ˚C. It is impossible to test at higher temperatures without considering the airflows needed, because the heaters purchased for this project only heat up to 400 ˚C and higher temperatures are only achieved by reducing the airflow.[34] Since the SOFC/GT system exhaust turbine space may only be modified to certain parameters, the valve's design must adhere to specific dimensions that cannot be exceeded, such as a height of 5 inches. NETL will prepare the system by reducing the diameter to a 3-inch valve structure and reducing the length of the size of the drilled hole to install the valve. In the previous study, it was able to be demonstrated that the shape memory alloy springs can function as valve actuators at room temperature testing. The high temperatures of the system require the use of a different production method and other materials than the room temperature designs.

Table 16: Room Temperature Lab Prototype Boundary Conditions

Fluid	Air
Volumetric Flow Rate	60 L/min – 80 L/min
Temperature	650˚C
Valve Material	Stainless Steel 304

4.3 DESIGN APPROACH

The next figures show the design that will be applied in the 8-inch pipe of the exhaust of the turbine located on the SOFC/GT system. The figures show a representation of how the designed part will look like after it is manufactured and installed in the facility. The cylinder in the figure represents the pipe in the NETL facility. The high-temperature design was made, by taking into consideration the room temperature designs. The changes made were done to facilitate the SMA springs installation and actuation. The team went on to have the SMA springs chamber to be expanded in a vertical direction for easy fabrication and the addition of a cooling system to prevent the springs from overheating and compromising their workability. The disc dimension is a 3-inch diameter. To reinstate, the goal of this project is only to redirect a small portion of the flow that goes towards a turbine and heat exchanger.

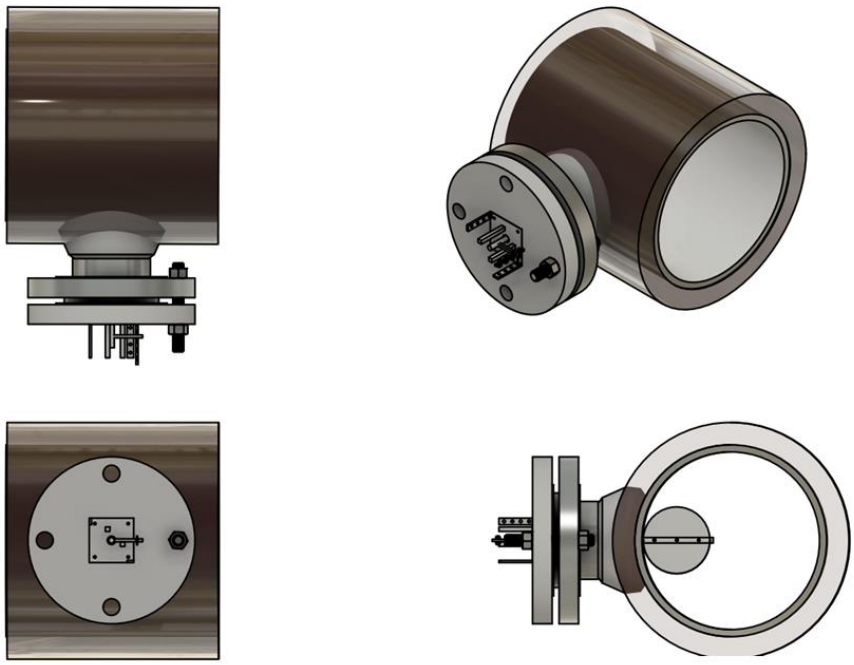

Figure 13: Valve Design for the Hyper Facility

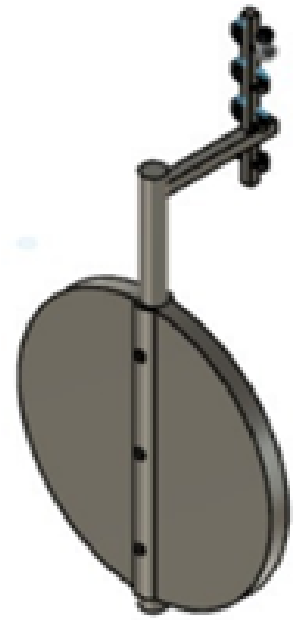

Figure 14: Rod and Disc Design for the Hyper Facility

Due to the fact that in the laboratory there is not that many things to be able to manufacture the whole piece on our own. The team searched outside workshops for the design to be fabricated. After several calls to different workshops and asking for quotes to manufacture said design. Larks

Industries, a machine shop located in El Paso, Texas, was contacted for the job. The final manufactured part was done in stainless steel 304, with a 0.5mm tolerance and a matt finish, as seen in figure 4.3.3 and figure 4.3.4. The benefits taken out of this design are that is high-temperature resistant, lightweight, corrosion resistant, pressure resistant, durable, has no leaks, and is more spacious on top for SMA installation.

Figure 15: Manufactured High-Temperature Design

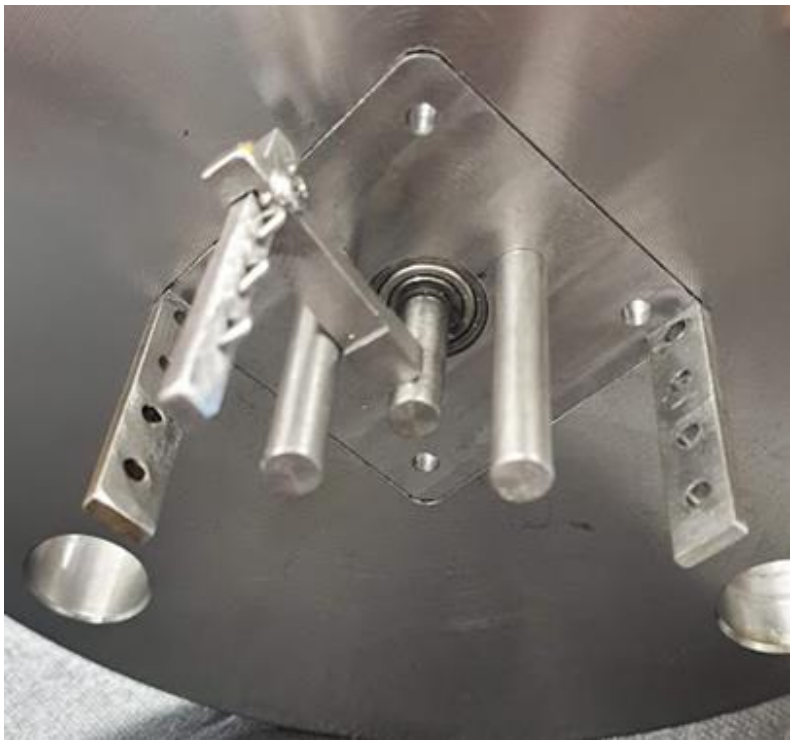

Figure 16: Top View Where SMA Springs are Installed

4.4 Safety Analysis

Chapter 3 safety analysis also is taken into consideration for this chapter. When working in a laboratory with a high-temperature project, one must take several precautions, as one does for any other research project. In the case of this chapter, a design documentation was made containing all the tools and equipment used while building and testing the prototype of the final design that will be installed in the SOFC/GT system. Quarterly reports were done throughout the whole project's timeline. Inside this documentation, it was briefly stated the status of the project as well as the test results to inform the project sponsors of the progress of the project. Any type of testing was beforehand discussed and analyzed to understand how it should be operated and what type of data is taken out. Before shipping out the design to the NETL facility, the team wrote down made a document with a brief description of how the valve needs to be installed in the HYPER facility.

All this is made for the person that will be installing the valve to have an idea of how it needs to be done and how it will work.

4.5 SMA Actuation Results

The actuation was tested by doing lab trials on the SMA installation with different electrical inputs before installing the valve into the HYPER facility. This was done to test out the workability of the SMA springs on the design and for the team to conclude which parts of the design will be needed to be insulated to have the SMA springs work perfectly. Figure 17 shows how the springs are installed and the approach the team took on calculating the time vs. position results. The angles were placed on the valve top, and time was recorded with a stopwatch.

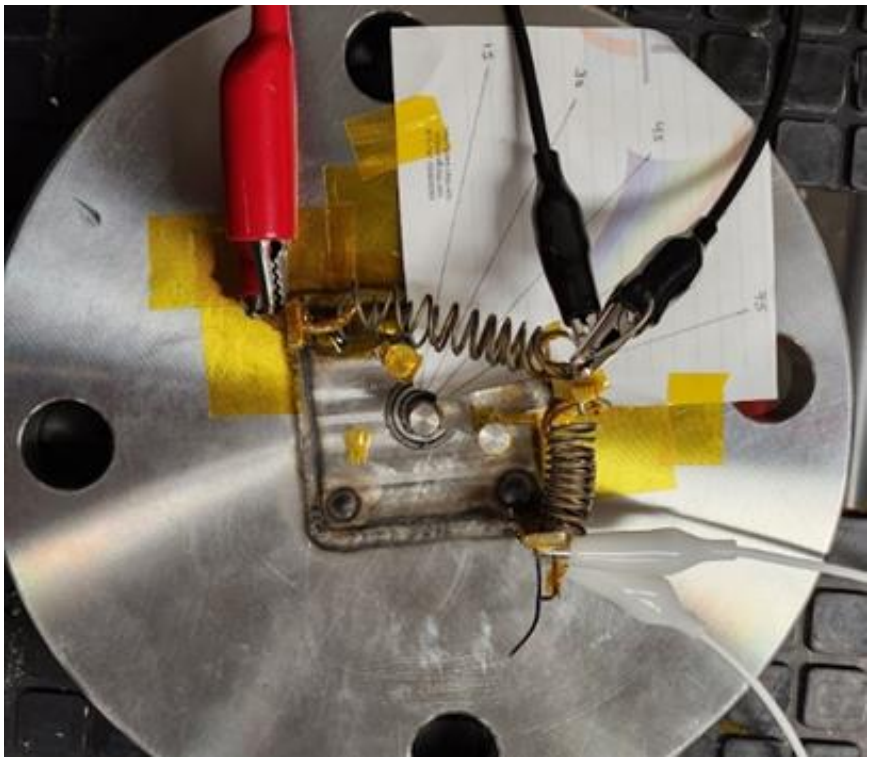

Figure 17: Shape Memory Alloy Springs Installation

For the opening and closing of the valve, it is needed to rotate from 0º to 90º. So, it was marked with a 15º interval, and the time required to reach each checkpoint was measured [Table 17 and Table 18].

Table 17: Measured Times at Different Angles (10amp – 6amp)

Position	10amp		8amp		9amp		7amp		6amp	
in degree	Time/15°	Total time	Time/15°	Total time	Time/15°	Total time	Time/15°	Total time	Time/15°	Total time
0	0.8	0.8	1.2	1.2	1.9	1.9	2	2	1.6	1.6
15	0.7	1.5	1.1	2.3	0.5	2.4	0.8	2.8	1.3	2.9
30	0.3	1.8	0.25	2.55	0.3	2.7	0.5	3.3	1.5	4.4
45	0.15	1.95	0.2	2.75	0.25	2.95	0.2	3.5	0.65	5.05
60	0.15	2.1	0.2	2.95	0.25	3.2	0.2	3.7	0.65	5.7
75	0.3	2.4	0.55	3.5	0.3	3.5	0.25	3.95	0.7	6.4
90	0.45	2.85	0.8	4.3	0.4	3.9	0.4	4.35	0.75	7.15

Table 18: Measured Times at Different Angles (5amp – 2amp)

Position	5amp		4amp		3amp		2amp	
in degree	Time/15°	Total time	Time/15°	Total time	Time/15°	Total time	Time/15°	Total time
0	8	8	6.5	6.5	14	14	22	22
15	2.5	10.5	2.25	8.75	7	21	22	44
30	1.5	12	2.25	11	6	27	24	68
45	1.25	13.25	2.25	13.25	3.25	30.25	24	92
60	1.25	14.5	2.25	15.5	3.25	33.5	15	107
75	1.5	16	2.25	17.75	3.5	37	11	118
90	2	18	3	20.75	4	41	9	127

Graphs 4 and 5 display the results of actuation speed with a constant voltage of 5 volts and a range of electrical currents from 2 to 10 amperes. With an increase in electrical current, the actuation time gradually shrank, with the lowest time recorded begin 2.85 seconds. Additionally, it was observed that although the valve's actuation time decreased as electrical input increased in steps, it did not change noticeably after applying 7 amperes, with 7amps taking 4.35 seconds. Compared to other portions, the actuation time is noticeably slower at the beginning 30°. This is due to the fact that it takes some time to produce the heat required for the shape memory alloy springs to begin actuating.

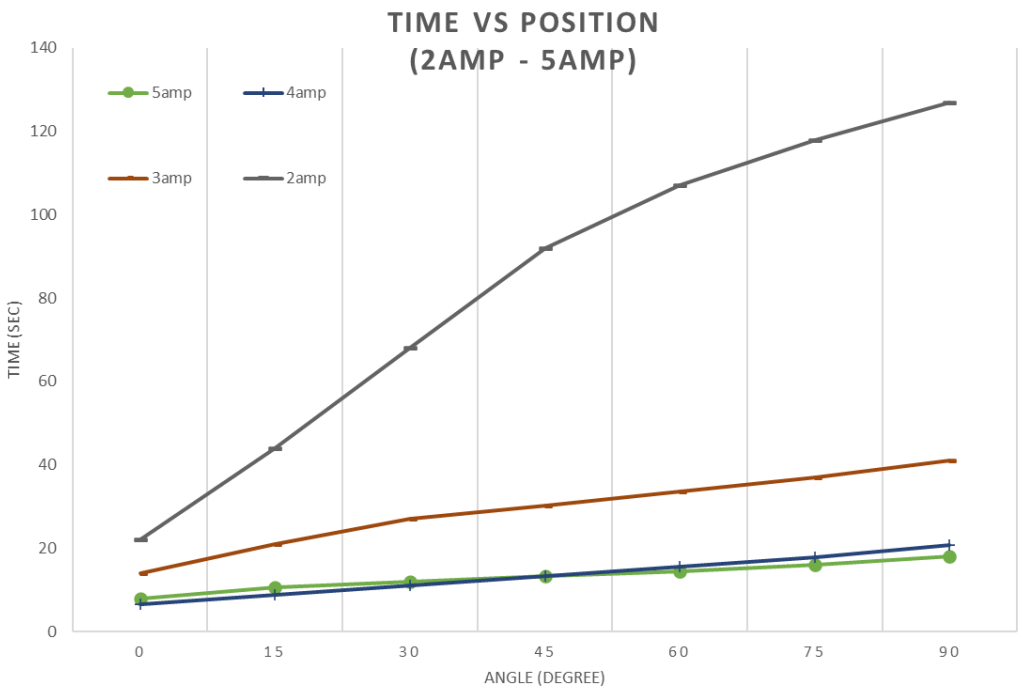

Graph 4: Time vs Position Graph from 2 amps to 5 amps

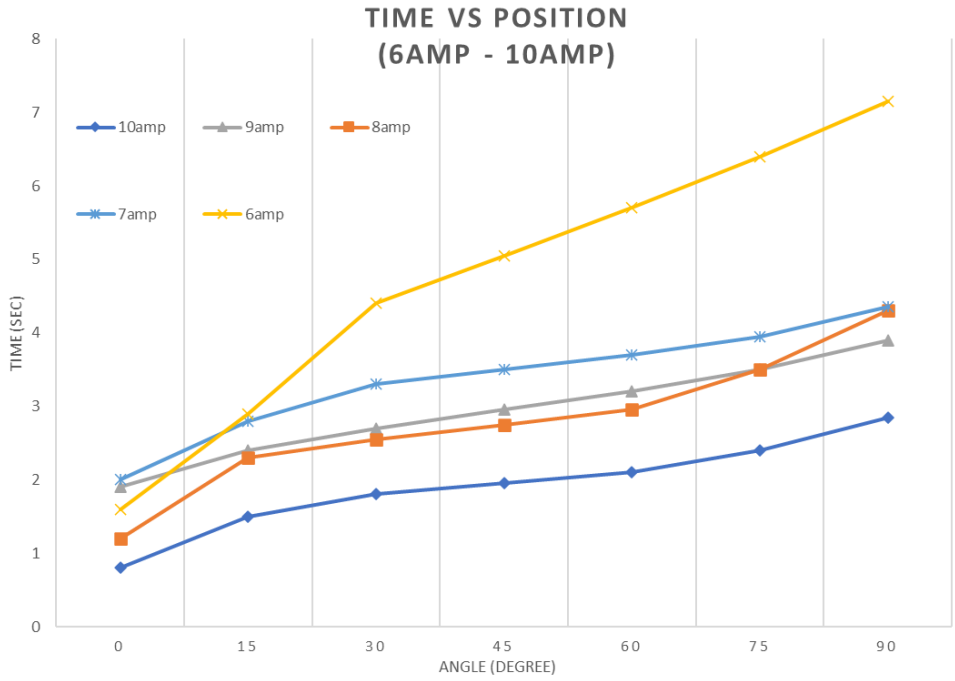

Graph 5: Time vs Position Graph from 6 amps to 10 amps

4.6 CONCLUSION

The study proposes a high-temperature, and pressure bypass valve to control the airflow going towards a turbine and heat exchanger during the startup of a Solid Oxide Fuel Cell/Gas Turbine (SOFC/GT) hybrid system. To control the high temperatures that are exhausted from the post-combustor, the bypass valve will be placed before the heat exchanger to regulate the airflow going to the fuel cell and avoid thermal stress on the material.

The final manufactured design was tested in laboratory conditions and presented before installation in the Hyper facility. The SMA springs' mechanical characteristics were identified. The spring compression time is dependent on the electrical inputs that are delivered, and it significantly decreases as the electrical current increases. The fastest reported actuation time used a 5-volt, 10-amp D.C. electrical source, and it was roughly 2.85 seconds. The testing outcomes have demonstrated that a valve system's SMA can be addressed in order to regulate airflow upon actuation. The manufactured design was proven successful and is ready to be shipped out for installation at the NETL HYPER facility.

This project's significance lies in its ability to inspire new high-temperature valve development concepts. The likelihood of responding to changes and finding new possibilities rises with innovation. This research generates fresh concepts that can be applied to numerous different SOFC/GT hybrid system tests, each of which serves a distinct project objective and aids in its accomplishment.

4.6.1 Future Work and Recommendations

For future work, the stainless-steel manufactured valve will be installed and tested at a high-temperature environment in the actual SOFC/GT system. The team will visit the facility to help with the installment of the valve to the system and see the actual SOFC/GT system working.

Since the designed disc for the stainless-steel valve is 3-in in diameter, after installation and recording the actual flow that is being redirected with the valve, the team can go ahead and design a bigger disc to bring up the redirect flow to be greater.

For the shape memory alloys to later on just utilize one spring instead of multiple for actuation, 2-way shape memory alloy springs can be researched and tested on the valve for actuation. A cooling chamber will be needed to be designed and placed on top of the design, where the shape memory alloys are installed, to have better control of the environment the springs are subjected to for them to work perfectly fine during the closing and opening of the valve.

SECTION 2: ADDITIONAL PROJECT

Chapter 1: Nanoindentation System Repair

In this chapter, you will read about what is nanoindentation testing and how the team will be applying this material characterization machine to different ongoing projects at the research laboratory. As the name of the chapter says, several issues were encountered at the beginning, and several pieces on the system needed to be changed to have the nanoindenter up and running again. This project was taken as an addition to the one presented in section 1.

1.1 Background and Introduction

Over the past ten years, nanoindentation has gained popularity as a mechanical characterization tool. Nanoindentation enables the measurement of mechanical properties such as the modulus of elasticity and hardness of materials in different shapes, sizes, and scales. All of this is possible with known indenter geometry and material properties.[35] The indentation test technique evaluates the mechanical properties of the specimens by diving an indenter tip into the specimen surface and then imaging the impression. The local elastic modulus and hardness are determined by applying contact mechanics analysis to the acquired force-depth response.[36] Nanoindentation is widely used to assess bulk material [37], interfaces in composites [38], nanostructured materials [39], thin films [40], and coatings [41]. That is why it is of major importance to understand the fundamentals of the mechanical properties tested by nanoindentation.

Nanoindentation has many advantages. In addition to young modulus and hardness, it can also be used to characterize other nanoscale mechanical properties such as shear strength [42], creep [43], and fracture toughness [44]. The local characteristics of both homogeneous and heterogeneous materials can be identified through nanoindentation. Due to the decrease in

specimen size restrictions, the method has been widely applied to items where the manufacturing conditions do not provide sufficient material for microhardness testing.

Elastic modulus can only be calculated using nanoindentation techniques on smooth, isotropic solids. The indented material's surface ought to be totally level and adjusted to the indenter tip. The surface finish will have a significant impact on the results of the nanoindentation because the indentation thicknesses are in the nanoscale range. On the other hand, getting a perfectly smooth surface is a difficult task. The indentation should be performed to a maximum depth of approximately 20 times the surface roughness in order to mitigate the effects of irregularity.[45]

1.2 PROCESS

Nanoindentation is an effective approach in which a defined indentation tip is pushed into a specific location on the test sample, a force is applied, and the load is gradually unloaded until the required depth is reached. A rest section is provided for materials to relax before unloading. The operation can be done repeatedly, with increasing loads for each indent.

1. A calibrated indenter tip approaches the surface sample
2. The force-displacement data recorded is used to determine the point of contact
3. Once the sample is contacted, the force is linearly increased and the tip indents into the sample’s surface.
4. The tip is held down at the maximum force for some time then the sample is unloaded.
5. At the initial point of unloading, the stiffness is measured.
6. The resulting load and displacement data along with the area from the calibrated indenter tip allow for the determination of mechanical properties such as elastic modulus and hardness.

Chapter 2: Theory

The test material, the sensors, and actuators used to apply and monitor the mechanical stress and indenter displacement, as well as the indenter tip, are the main elements of a nanoindentation experiment. The final part is often composed of diamond and shaped into a sharp, symmetrical shape, like the three-sided Berkovich pyramid as shown in figure 18.[46] The applied test force and the indenter's depth are continually monitored during an instrumented indentation test. Diamond, tungsten carbide, and sapphire are examples of typical indenter materials. Indenter geometries that are commonly utilized include pyramidal with a square base (Vickers), pyramidal with a triangular base (Berkovich and cube corner), and spherical, figure 18. Nanoindentation analysis is straightforward, but data interpretation can be difficult. One of the most difficult tasks is choosing the right indenter tip for the job and currently interpreting the results. That is why choosing the correct tip for your tested material is really important.

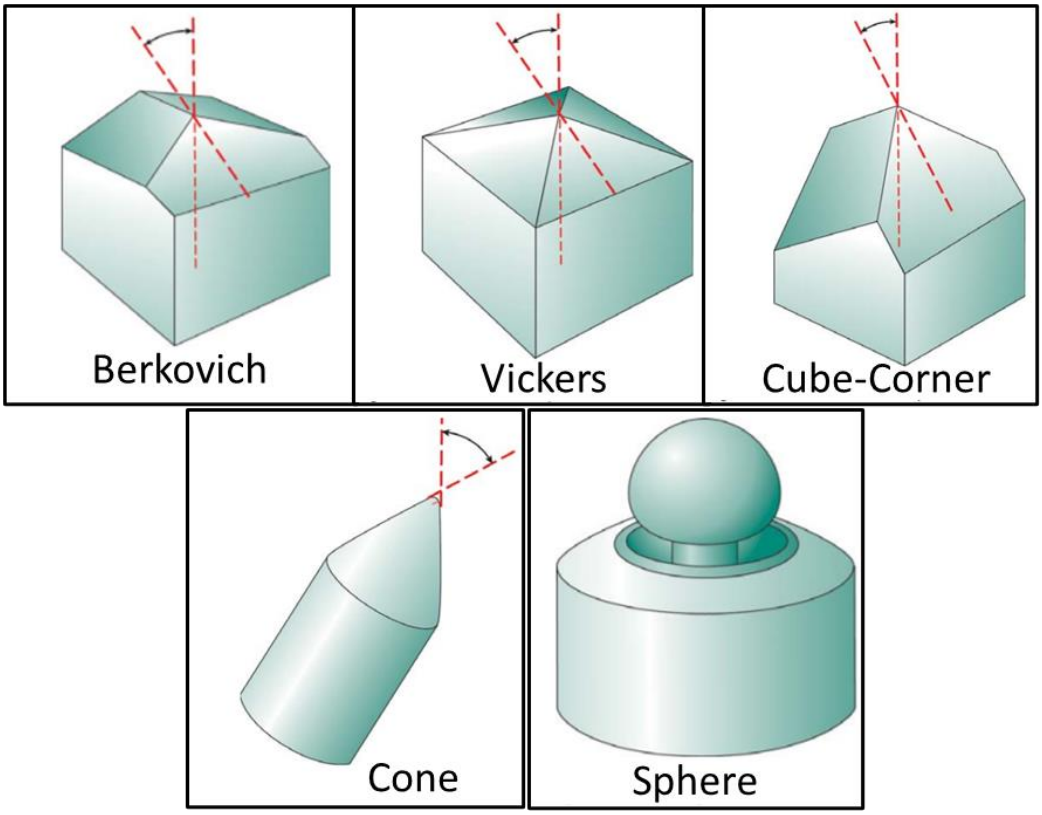

Figure 18: Types of Indenter Tips[47]

Each tip comes with different properties designed to meet any kind of application.[48] The different kinds of tips can be separated into sharp and blunt indenter types, depending on the material you are planning to indent and the benefits you want to obtain from the tip, you can go ahead and choose the tip that goes perfectly with your application, as seen on figure 19 and table 19.

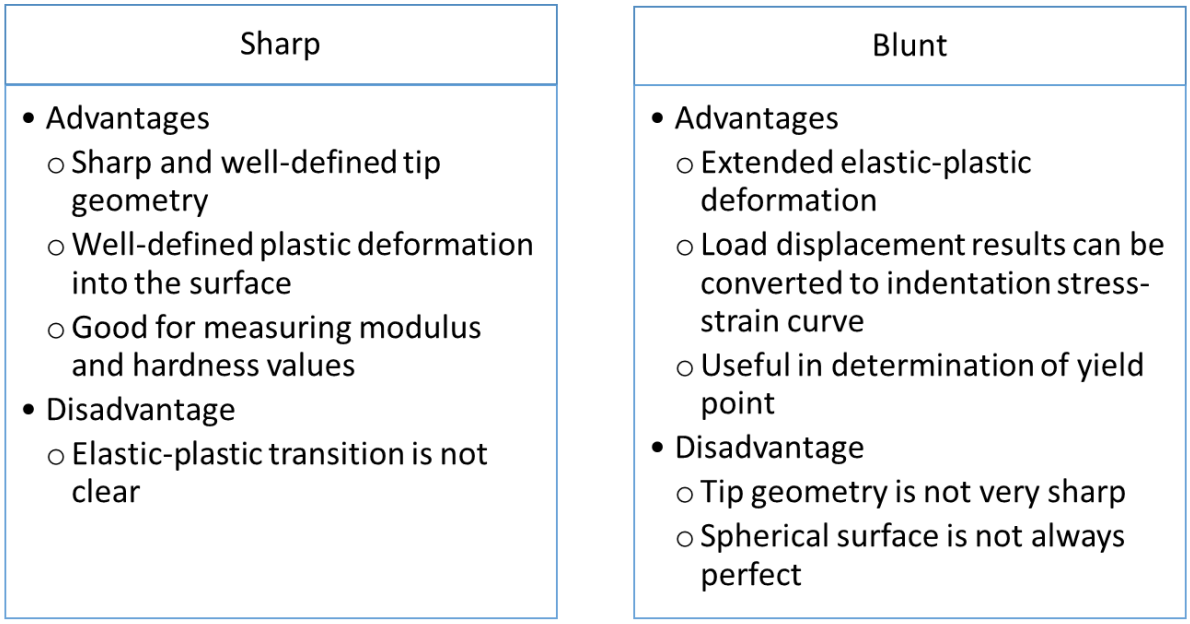

Figure 19: Difference Between Sharp and Blunt Tips

Table 19: Indenter Types Characteristics for Calculations

Indenter Type		Projected area	Semi angle (Θ)	Effective cone angle (α)	Intercept factor	Geometry correction factor (β)
Blunt	Sphere	$A = \pi 2Rh_p$	N/A	N/A	0.75	1
Sharp	Berkovich	$A = 3h_p^2 tan^2\theta$	65.3	70.2996	0.75	1.034
	Vickers	$A = 4h_p^2 tan^2\theta$	68	70.32	0.75	1.012
Blunt	Cone	$A = \pi h_p^2 tan^2\alpha$	α	α	0.72	1

Nanoindentation involves making contact with a sample surface using an indenter tip while measuring the force and displacement. A typical nanoindentation curve can be broken down into two stages: loading and unloading. The first stage pushes the tip into the sample by increasing the load. This can lead to both elastic and plastic deformation. The force peak was reached as the maximum depth displacement. This is followed by an unloading phase during which the elastic deformation is restored.[49]–[51] In a typical nanoindentation test, forces and displacements are recorded when the indenter tip is pressed against the surface of the test material with a given load and load profile. The response to this test is the load-displacement curve as seen in graph 6.

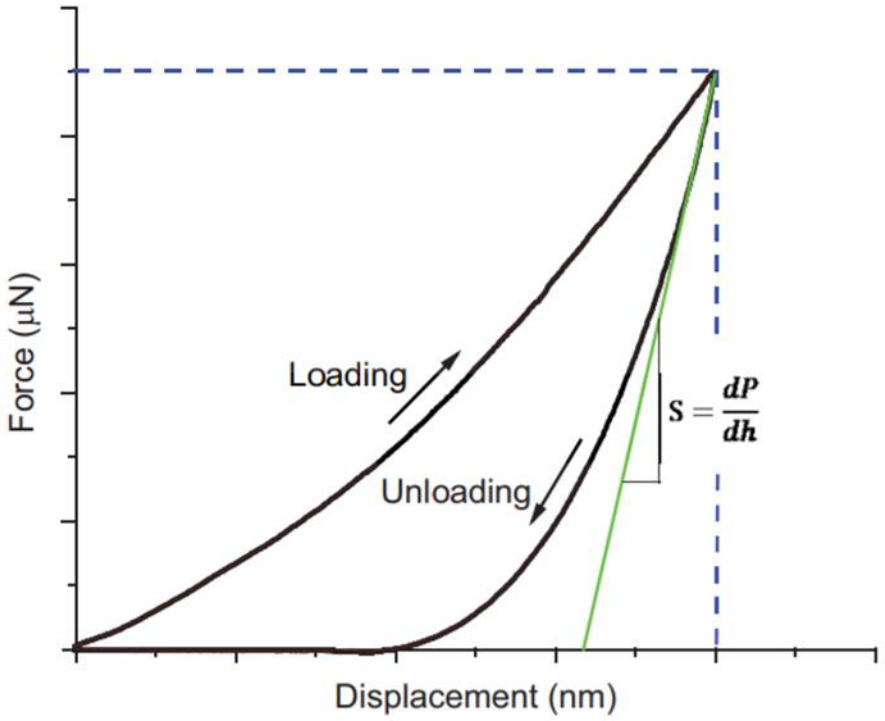

Note: Srepresents Young's modulus

Graph 6: Typical Load-Displacement Curve in a Nanoindentation Test[49]

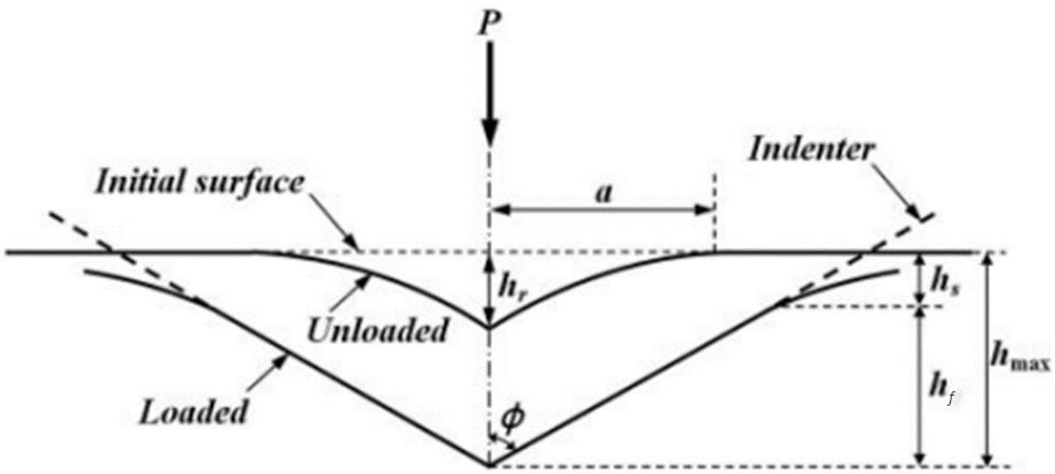

Figure 20: Schematic Illustration of the Unloading Process in Nanoindentation[52]

2.1 Calculation Method

In recent decades, various methods have been developed to analyze nanoindentation curves.[53]–[55] The most common method to determine the modulus and hardness of any material is based on the work of Oliver and Pharr.[56] Following this procedure, the hardness of the nanoindentation as a function of the final penetration depth of the indentation can be determined by the following equation:

$$H = \frac{P_{max}}{A}$$

Where P_{max} is the maximum applied load measured at the maximum depth of penetration (h_{max}), A is the projected contact area between the indenter and the specimen. Considering a perfect Berkovich indenter tip, A can be defined as a function of the contact indentation depth h_f as:

$$A = 3\sqrt{3}h_f^2 tan^2 65.3 = 24.5h_f^2$$

The contact indentation depth, h_f, can be determined from the following expression:

$$h_f = h_{max} - \varepsilon\frac{P_{max}}{S}$$

Where the geometric constant, ε, is equal to 0.75 for a pyramidal indenter. The contact stiffness, S, is determined as the slope of the unloading curve at the maximum loading point,

$$S = (\frac{dP}{dh})_{h=h_{max}}$$

The reduced elastic modulus E_r is determined by:

$$E_r = \frac{S}{2\beta}\sqrt{\frac{\pi}{A}}$$

Where β is a constant dependent on the shape of the indenter. For a Berkovich indenter tip, β is equal to 1.034. The samples elastic modulus, E_s, can then be calculated as:

$$\frac{1}{E_r} = \frac{1 - v_s^2}{E_s} + \frac{1 - v_i^2}{E_i}$$

Where the elastic modulus and Poisson's ratio are $E_{i,s}$ and $v_{i,s}$, respectively, for the sample and indenter. For a Berkovich diamond indenter $E_{i,s}$ is equal to 1140 GPa and $v_{i,s}$ is equal to 0.07.[56], [57]

Chapter 3: Troubleshooting and Maintenance

The nanoindentation system used in the laboratory is the Nanoindenter Hysitron TI 750 Ubi, by Bruker Company. The picture below shows an image of the system in question.

Figure 21: Nanoindenter Hysitron TI 750 Ubi System

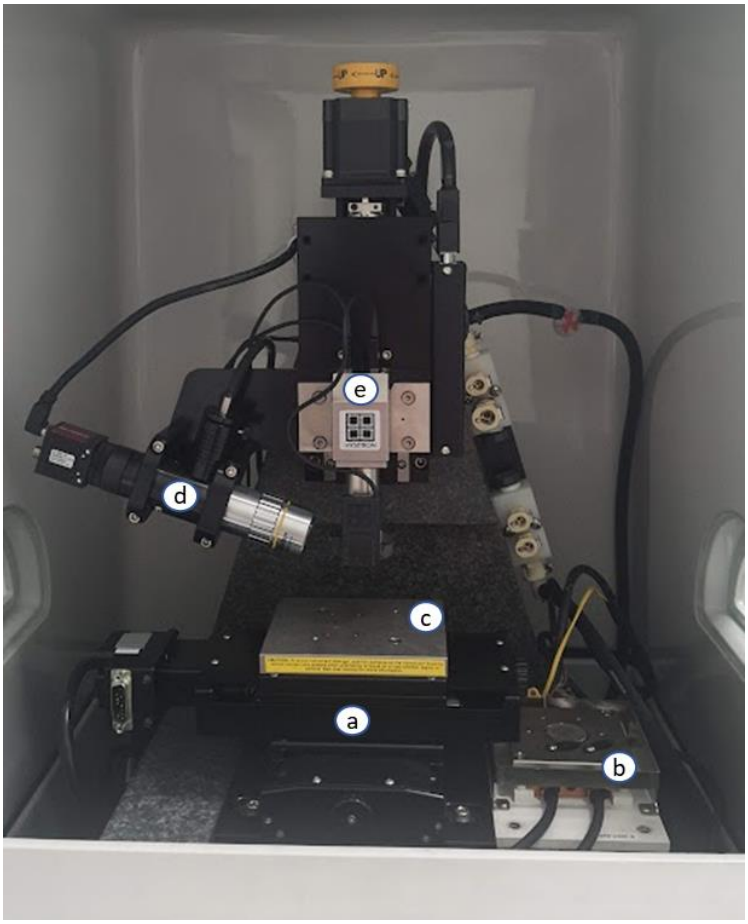

Figure 22: Inside Look of Nanoindenter System; a. XY Stages, b. High-Temperature Sample Stage, c. Sample Stage, d. Optical Camara System, e. Piezo Transducer

The system is 11 years old, and previous research teams working with it used it improperly when testing. As a result, when going back to applying this characterization machine to the ongoing projects, the team had to contact a Bruker specialist for help fixing the system. Troubleshooting went easy and quick in determining the source of the issues at hand. One main issue that was encountered was that the system had not been calibrated regularly. When doing this calibration after many years have passed, it was seen that the Berkovich tip installed in the system was not responding the way it is supposed to. From here on, a quartz sample was indented using that same Berkovich tip to have a look at the response and its load-displacement curve. By looking at the results and sharing them with the Bruker representative it was clear that the tip became blunt,

losing its sharper characteristics to get nice results. By looking into this the team moved into purchasing a new Berkovich tip as well as a Flat Punch Tip to use when testing different materials.

When the first characterization tests began, it was noticed that the machine was not moving easily and that the XY platform stages were getting stuck now and then. The team quickly contacted the Bruker representative to notify them about this issue and how to go approach a solution. The stages then needed to be removed and sent to Bruker headquarters to be properly lubricated and revised for them to work without any issues. The stages were safely returned to the laboratory and installed back into the system. One last modification that was set up on the system was the purchase of a new piezotransducer scanner, this part is the one that indents into the sample and records the results on load and displacement. This piece was changed to have a bigger range on the sample stage for more samples to be tested at the same time in the same run.

After all the troubleshooting and maintenance were done, the nanoindenter is now ready to be used for testing

Chapter 4: Lab Tests

In this chapter, it is discussed the achieved data taken from nanoindentation testing of hollow polysiloxane microspheres. These spheres were created to fabricate syntactic foams.[58] Polysiloxanes, also known as silicones, are a general category of polymers that have organic groups, typically methyl groups, attached to the silicon atoms. They have a silicon-oxygen backbone.[59] Syntactic foam gets its low density, high specific strength, low moisture absorption, and other properties from the hollow microspheres. Syntactic foam microspheres have a burst pressure that is strong enough to withstand the forces that are applied to them during the formulation, mixing, and dispensing procedures. The fact that systems with spherical fillers always have a lower viscosity than systems with fillers of any other shape is one of the main benefits of

microspheres. Depending on the material, microspheres can withstand high temperatures, have high strength-to-weight ratios, clean surface chemistry, a narrow distribution of particles, low thermal conductivity, low dielectric constant, low dissipation factor, etc., which makes them an essential material for strengthening. The density, wall thickness, and size of the particles make up the characteristics of micro balloons. Syntactic foam microspheres typically have a diameter between 1 and 50 m, a wall thickness between 1 and 4 m, a bulk density between 70 and 500 kg/m3, and an apparent density between 50 and 500 kg/m3.[60], [61]

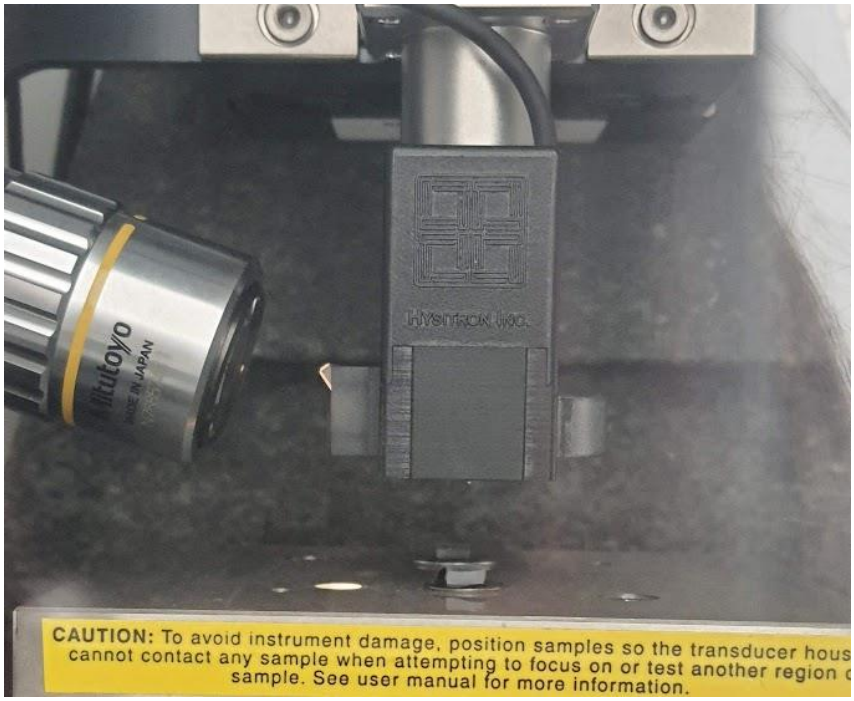

Figure 23: Nanoindentation Testing of Hollow Polysiloxane Microspheres

4.1 Hollow Particles Characterization

Four samples of hollow Polysiloxane spheres were characterized using nanoindentation. Graph 7 shows the load displacement curve for the 4 samples. These indentations were done with a Berkovich tip, as seen it does not look like the typical load- displacement curve shown in graph 6. This is because the tests were done when the machine was still not up and running correctly, the indenter tip used was blunt resulting in terrible readings.

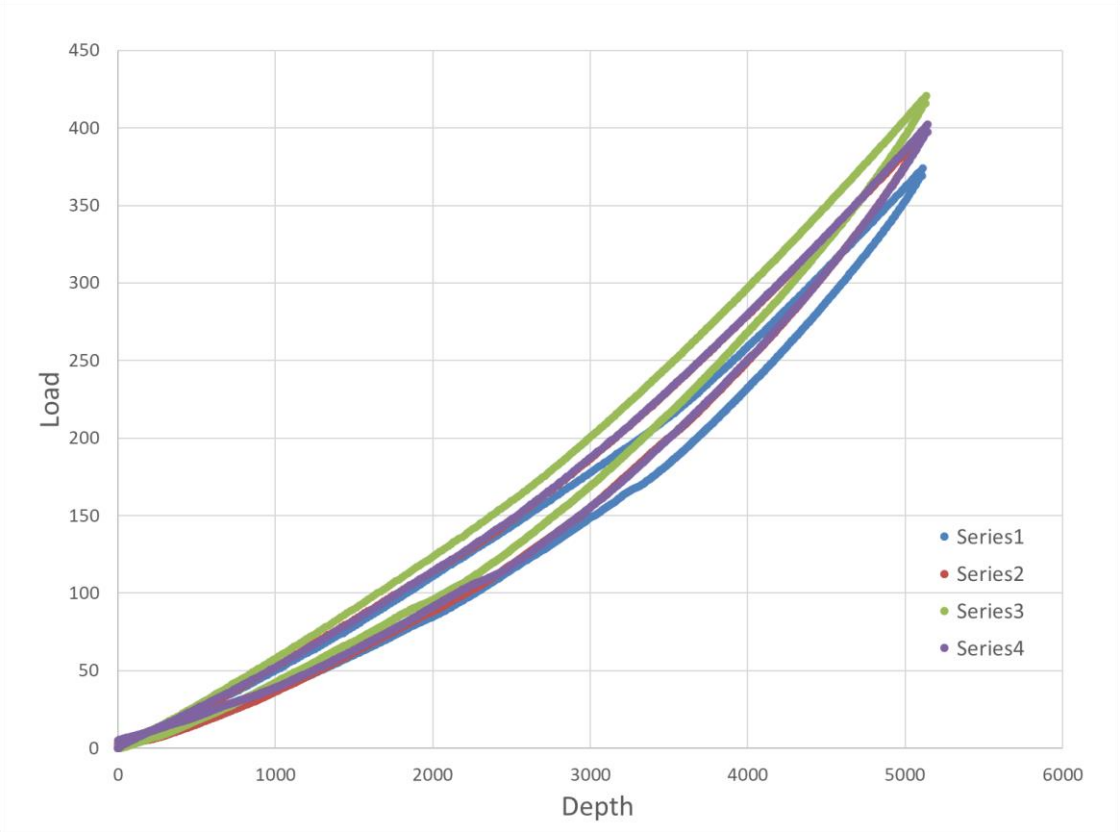

Graph 7: Load-Displacement Curve for Hollow Particles Indentation

By following the results given on the graph above and by following the next figure to help analyze the data collected. It is given that the sample do have a hysteresis response while being indented. It is noticed that there are also no sudden compliance changes while recording the data. As seen on the graph the hysteresis changes with the rate making it go back to 0 on the displacement as the load decreases. One can also state by looking at the results that there is no sign of residual deformation not recovering due to the indentation. By having all those facts taken from the graph and looking at the figure below, the hollow particles indentation test result on the sample tested to have a viscous elastic deformation. The team believes that these kinds of results were achieved due to the fact of indenting with a blunt tip and for the state of the system when doing these tests.

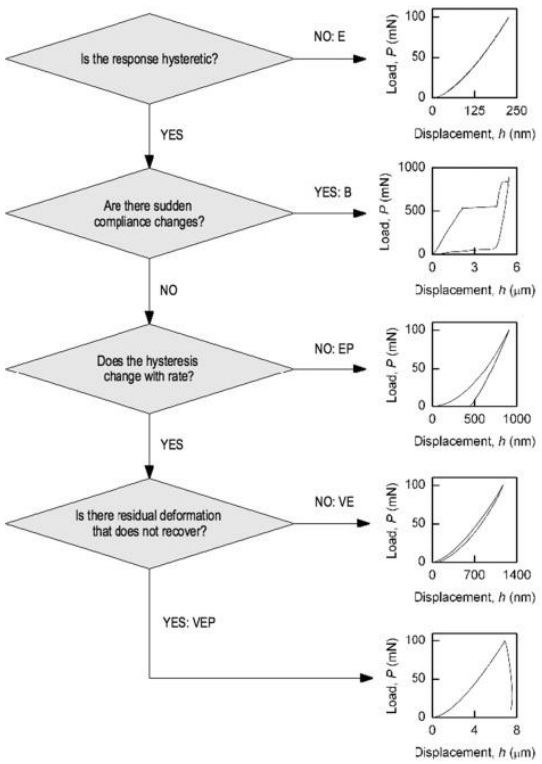

Figure 24: A decision tree structure for identifying dominant modes of deformation in instrumented indentation load–displacement data [62] E, elastic; B, brittle; P, plastic; V, viscous

Chapter 5: Conclusion

In conclusion, the nanoindentation system proved to be a good material characterization for hardness and elastic modulus. The team was able to get some decent results when indenting hollow polysiloxane microspheres. After those results, the system went under maintenance again for a few days, and is up and running perfectly now.

5.1 Future Work and Recommendations

For future work, nanoindentation characterization will still be used for indenting hollow particles with a Berkovich tip as well as a Flat Punch tip. The data gotten from both tips will later on be compared and analyzed to see which one is best for indenting on hollow particles. Since the laboratory has many other projects taking place, it is recommended to take advantage of this characterization system and use it in different materials, such as 3D-printed polymers and ceramics. Once good and correct data is recorded, the hardness and young's modulus of the specimens tested with respect to the load-displacement curve will be calculated.

References

[1] S. E. Veyo, L. A. Shockling, J. T. Dederer, J. E. Gillett, and W. L. Lundberg, "Tubular solid oxide fuel cell/gas turbine hybrid cycle power systems: Status," *J Eng Gas Turbine Power*, vol. 124, no. 4, pp. 845–849, Oct. 2002, doi: 10.1115/1.1473148.

[2] B. Zhang *et al.*, "Rapid load transition for integrated solid oxide fuel cell – Gas turbine (SOFC-GT) energy systems: A demonstration of the potential for grid response," *Energy Convers Manag*, vol. 258, Apr. 2022, doi: 10.1016/j.enconman.2022.115544.

[3] S. Mohith, A. R. Upadhya, K. P. Navin, S. M. Kulkarni, and M. Rao, "Recent trends in piezoelectric actuators for precision motion and their applications: a review," *Smart Mater Struct*, vol. 30, no. 1, p. 013002, Jan. 2021, doi: 10.1088/1361-665X/abc6b9.

[4] V. Apicella, C. S. Clemente, D. Davino, D. Leone, and C. Visone, "Review of Modeling and Control of Magnetostrictive Actuators," *Actuators*, vol. 8, no. 2, p. 45, May 2019, doi: 10.3390/act8020045.

[5] F. K. Straub and D. J. Merkley, "Design of a smart material actuator for rotor control," *Smart Mater Struct*, vol. 6, no. 3, pp. 223–234, Jun. 1997, doi: 10.1088/0964-1726/6/3/002.

[6] Boiler & Mechanical Power, "Types of Valves and Their Classification," *Boilersinfo*, 2022. https://boilersinfo.com/types-of-valves-with-images/ (accessed Nov. 12, 2022).

[7] Assured Automation, "Types of Valves," *ASSURED AUTOMATION*. https://assuredautomation.com/actuated-valve-training/types-of-valves.php (accessed Nov. 12, 2022).

[8] O. Abdulhameed, A. Al-Ahmari, W. Ameen, and S. H. Mian, “Additive manufacturing: Challenges, trends, and applications,” *Advances in Mechanical Engineering*, vol. 11, no. 2, p. 168781401882288, Feb. 2019, doi: 10.1177/1687814018822880.

[9] K. v. Wong and A. Hernandez, “A Review of Additive Manufacturing,” *ISRN Mechanical Engineering*, vol. 2012, pp. 1–10, Aug. 2012, doi: 10.5402/2012/208760.

[10] P. K. Penumakala, J. Santo, and A. Thomas, “A critical review on the fused deposition modeling of thermoplastic polymer composites,” *Compos B Eng*, vol. 201, p. 108336, Nov. 2020, doi: 10.1016/j.compositesb.2020.108336.

[11] M. S. Hassan *et al.*, “Selective Laser Sintering of High-Temperature Thermoset Polymer,” *Journal of Composites Science*, vol. 6, no. 2, p. 41, Jan. 2022, doi: 10.3390/jcs6020041.

[12] L. del-Mazo-Barbara and M.-P. Ginebra, “Rheological characterisation of ceramic inks for 3D direct ink writing: A review,” *J Eur Ceram Soc*, vol. 41, no. 16, pp. 18–33, Dec. 2021, doi: 10.1016/j.jeurceramsoc.2021.08.031.

[13] H. R. Kotadia, G. Gibbons, A. Das, and P. D. Howes, “A review of Laser Powder Bed Fusion Additive Manufacturing of aluminium alloys: Microstructure and properties,” *Addit Manuf*, vol. 46, p. 102155, Oct. 2021, doi: 10.1016/j.addma.2021.102155.

[14] D. Dev Singh, S. Arjula, and A. Raji Reddy, “Functionally Graded Materials Manufactured by Direct Energy Deposition: A review,” *Mater Today Proc*, vol. 47, pp. 2450–2456, 2021, doi: 10.1016/j.matpr.2021.04.536.

[15] M. Li, W. Du, A. Elwany, Z. Pei, and C. Ma, “Metal Binder Jetting Additive Manufacturing: A Literature Review,” *J Manuf Sci Eng*, vol. 142, no. 9, Sep. 2020, doi: 10.1115/1.4047430.

[16] J. Huang, Q. Qin, and J. Wang, “A Review of Stereolithography: Processes and Systems,” *Processes*, vol. 8, no. 9, p. 1138, Sep. 2020, doi: 10.3390/pr8091138.

[17] K. Otsuka and X. Ren, “Recent developments in the research of shape memory alloys,” *Intermetallics (Barking)*, vol. 7, no. 5, pp. 511–528, May 1999, doi: 10.1016/S0966-9795(98)00070-3.

[18] K. Otsuka and X. Ren, “Physical metallurgy of Ti–Ni-based shape memory alloys,” *Prog Mater Sci*, vol. 50, no. 5, pp. 511–678, Jul. 2005, doi: 10.1016/j.pmatsci.2004.10.001.

[19] G. Costanza and M. E. Tata, “Shape Memory Alloys for Aerospace, Recent Developments, and New Applications: A Short Review,” *Materials*, vol. 13, no. 8, p. 1856, Apr. 2020, doi: 10.3390/ma13081856.

[20] C. Wang *et al.*, “Additive manufacturing of NiTi shape memory alloys using pre-mixed powders,” *J Mater Process Technol*, vol. 271, pp. 152–161, Sep. 2019, doi: 10.1016/j.jmatprotec.2019.03.025.

[21] *Shape Memory Alloys*, vol. 1. Boston, MA: Springer US, 2008. doi: 10.1007/978-0-387-47685-8.

[22] J. Ma, I. Karaman, and R. D. Noebe, “High temperature shape memory alloys,” *International Materials Reviews*, vol. 55, no. 5, pp. 257–315, Sep. 2010, doi: 10.1179/095066010X12646898728363.

[23] M. Formentini and S. Lenci, “An innovative building envelope (kinetic façade) with Shape Memory Alloys used as actuators and sensors,” *Autom Constr*, vol. 85, pp. 220–231, Jan. 2018, doi: 10.1016/j.autcon.2017.10.006.

[24] M. Ansari, P. Fahimi, M. Baghani, and M. Golzar, “An Experimental Investigation on Training of NiTi-Based Shape Memory Alloys,” *Int J Appl Mech*, vol. 10, no. 04, p. 1850040, May 2018, doi: 10.1142/S1758825118500400.

[25] H. Y. Luo and E. W. Abel, “A comparison of methods for the training of NiTi two-way shape memory alloy,” *Smart Mater Struct*, vol. 16, no. 6, pp. 2543–2549, Dec. 2007, doi: 10.1088/0964-1726/16/6/058.

[26] G. K. Stylios and T. Wan, “Shape memory training for smart fabrics,” *Transactions of the Institute of Measurement and Control*, vol. 29, no. 3–4, pp. 321–336, Aug. 2007, doi: 10.1177/0142331207069479.

[27] J. R. Santiago Anadón, “LARGE FORCE SHAPE MEMORY ALLOY LINEAR ACTUATOR,” 2002.

[28] A. Jacobsen and N. B. Kristjánsdóttir, “Shape Memory Alloys.”

[29] J. Ma, H. Huang, and J. Huang, “Characteristics analysis and testing of SMA spring actuator,” *Advances in Materials Science and Engineering*, vol. 2013, 2013, doi: 10.1155/2013/823594.

[30] C. Liang and C. A. Rogers, “Design of shape memory alloy springs with applications in vibration control,” *J Intell Mater Syst Struct*, vol. 8, no. 4, pp. 314–322, 1997, doi: 10.1177/1045389X9700800404.

[31] C. Liang, “The Constitutive Modeling of Shape Memory Alloys,” Virginia Polytechnic Institute and State University, 1990.

[32] M. Formentini and S. Lenci, “An innovative building envelope (kinetic façade) with Shape Memory Alloys used as actuators and sensors,” *Autom Constr*, vol. 85, pp. 220–231, Jan. 2018, doi: 10.1016/j.autcon.2017.10.006.

[33] The Process Piping, “Introduction to Butterfly Valves,” *April 29, 2020*. https://www.theprocesspiping.com/introduction-to-butterfly-valves/ (accessed Nov. 07, 2022).

[34] N. Love, C. David Espalin, E. Smith, and S. L. Crites, “EFFECT OF TEMPERATURE ON A PIEZOELECTRIC MASS FLOW RATE SENSOR.”

[35] B. Poon, D. Rittel, and G. Ravichandran, “An analysis of nanoindentation in linearly elastic solids,” *Int J Solids Struct*, vol. 45, no. 24, pp. 6018–6033, Dec. 2008, doi: 10.1016/j.ijsolstr.2008.07.021.

[36] F. Bernachy-Barbe, “A data analysis procedure for phase identification in nanoindentation results of cementitious materials,” *Materials and Structures/Materiaux et Constructions*, vol. 52, no. 5, Oct. 2019, doi: 10.1617/s11527-019-1397-y.

[37] Z. H. Xu and D. Rowcliffe, “Method to determine the plastic properties of bulk materials by nanoindentation,” *Philosophical Magazine A: Physics of Condensed Matter, Structure, Defects and Mechanical Properties*, vol. 82, no. 10, pp. 1893–1901, 2002, doi: 10.1080/01418610208235701.

[38] R. F. Gibson, “A review of recent research on nanoindentation of polymer composites and their constituents,” *Composites Science and Technology*, vol. 105. Elsevier Ltd, pp. 51–65, Dec. 01, 2014. doi: 10.1016/j.compscitech.2014.09.016.

[39] H. H. Ruan, A. Y. Chen, and J. Lu, “Characterization of plastically graded nanostructured material: Part I. The theories and the inverse algorithm of nanoindentation,” *Mechanics of Materials*, vol. 42, no. 5, pp. 559–569, May 2010, doi: 10.1016/j.mechmat.2010.02.005.

[40] W. D. Nix, “Elastic and plastic properties of thin films on substrates: nanoindentation techniques,” 1997.

[41] S. J. Bull, “Nanoindentation of coatings,” *Journal of Physics D: Applied Physics*, vol. 38, no. 24. Dec. 21, 2005. doi: 10.1088/0022-3727/38/24/R01.

[42] H. Bei, Z. P. Lu, and E. P. George, “Theoretical Strength and the Onset of Plasticity in Bulk Metallic Glasses Investigated by Nanoindentation with a Spherical Indenter,” *Phys Rev Lett*, vol. 93, no. 12, p. 125504, Sep. 2004, doi: 10.1103/PhysRevLett.93.125504.

[43] C. Minnert and K. Durst, “Nanoindentation creep testing: Advantages and limitations of the constant contact pressure method,” *J Mater Res*, vol. 37, no. 2, pp. 567–579, Jan. 2022, doi: 10.1557/s43578-021-00445-6.

[44] M. Sebastiani, K. E. Johanns, E. G. Herbert, and G. M. Pharr, “Measurement of fracture toughness by nanoindentation methods: Recent advances and future challenges,” *Curr Opin Solid State Mater Sci*, vol. 19, no. 6, pp. 324–333, Dec. 2015, doi: 10.1016/j.cossms.2015.04.003.

[45] U. Ahmed, “What is Nanoindentation?,” *AZONANO*, 2022.

[46] C. A. Schuh, “Nanoindentation studies of materials,” *Materials Today*, vol. 9, no. 5, pp. 32–40, May 2006, doi: 10.1016/S1369-7021(06)71495-X.

[47] “How to Select the Correct Indenter Tip Support Note.”

[48] H. Bei, E. P. George, J. L. Hay, and G. M. Pharr, “Influence of indenter tip geometry on elastic deformation during nanoindentation,” *Phys Rev Lett*, vol. 95, no. 4, Jul. 2005, doi: 10.1103/PhysRevLett.95.045501.

[49] L. Kong, M. Ostadhassan, R. Lin, and C. Li, “Nanoscale mechanical properties of 3D printed gypsum-powder-based rocks by nanoindentation and numerical modeling,” *Rapid Prototyp J*, vol. 25, no. 7, pp. 1295–1308, Aug. 2019, doi: 10.1108/RPJ-07-2018-0162.

[50] Z. Hu, “Characterization of Materials, Nanomaterials, and Thin Films by Nanoindentation,” in *Microscopy Methods in Nanomaterials Characterization*, Elsevier, 2017, pp. 165–239. doi: 10.1016/B978-0-323-46141-2.00006-7.

[51] B. Bhushan, “Depth-sensing nanoindentation measurement techniques and applications,” *Microsystem Technologies*, vol. 23, no. 5. Springer Verlag, pp. 1595–1649, May 01, 2017. doi: 10.1007/s00542-017-3372-2.

[52] L. N. Zhu, B. S. Xu, H. D. Wang, and C. B. Wang, “Measurement of residual stresses using nanoindentation method,” *Critical Reviews in Solid State and Materials Sciences*, vol. 40, no. 2. Taylor and Francis Inc., pp. 77–89, Mar. 04, 2015. doi: 10.1080/10408436.2014.940442.

[53] K. K. Jha, N. Suksawang, D. Lahiri, and A. Agarwal, “A novel energy-based method to evaluate indentation modulus and hardness of cementitious materials from nanoindentation load–displacement data,” *Materials and Structures/Materiaux et Constructions*, vol. 48, no. 9, pp. 2915–2927, Sep. 2015, doi: 10.1617/s11527-014-0367-7.

[54] Y. T. Cheng and C. M. Cheng, “Scaling approach to conical indentation in elastic-plastic solids with work hardening,” *J Appl Phys*, vol. 84, no. 3, pp. 1284–1291, Aug. 1998, doi: 10.1063/1.368196.

[55] S. v Hainsworth and T. F. Page, “Nanoindentation studies of the chemomechanical effect in sapphire,” 1994.

[56] W. C. Oliver and G. M. Pharr, “An improved technique for determining hardness and elastic modulus using load and displacement sensing indentation experiments,” *J Mater Res*, vol. 7, no. 6, pp. 1564–1583, Jun. 1992, doi: 10.1557/JMR.1992.1564.

[57] X. Li and B. Bhushan, “A review of nanoindentation continuous stiffness measurement technique and its applications.”

[58] Y. Lin, C. Sabrina Torres, T.-L. Tseng, and S. L. Crites, “SYNTHESIS, CHARACTERIZATION, AND DIRECT-INK-WRITING OF SYNTACTIC FOAMS ANDREA IRIGOYEN.”

[59] M. C. Hacker and A. G. Mikos, “Synthetic Polymers,” in *Principles of Regenerative Medicine*, Elsevier, 2011, pp. 587–622. doi: 10.1016/B978-0-12-381422-7.10033-1.

[60] B. John and C. P. Reghunadhan Nair, “Thermosetting polymer based syntactic foams: an overview,” in *Handbook of Thermoset Plastics*, Elsevier, 2022, pp. 801–832. doi: 10.1016/B978-0-12-821632-3.00020-8.

[61] B. John and C. P. Reghunadhan Nair, “Syntactic Foams,” in *Handbook of Thermoset Plastics*, Elsevier, 2014, pp. 511–554. doi: 10.1016/B978-1-4557-3107-7.00013-0.

[62] M. L. Oyen and R. F. Cook, “A practical guide for analysis of nanoindentation data,” *J Mech Behav Biomed Mater*, vol. 2, no. 4, pp. 396–407, Aug. 2009, doi: 10.1016/j.jmbbm.2008.10.002.

Glossary

Nitinol Shape Memory Alloy Springs

Prototype Testing Set Up

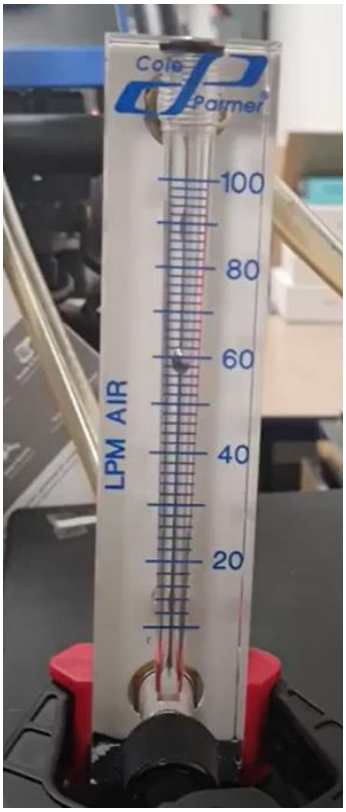

Mass Flow Meters used on Prototype

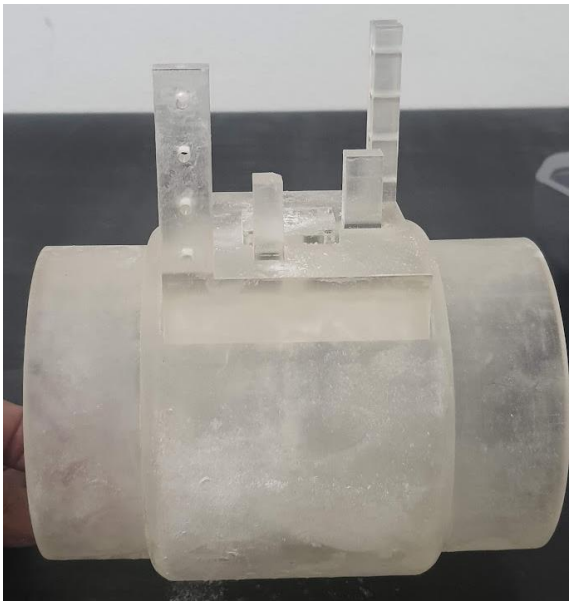

Clear Resin Design with the Same Top Design as High-Temperature Design

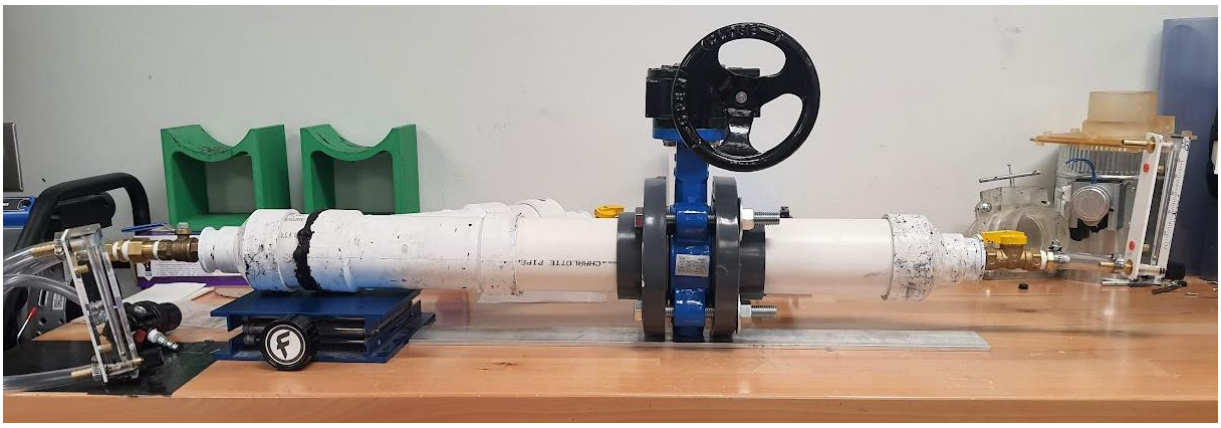

Actual Butterfly Valve Tested to Understand its Mechanism

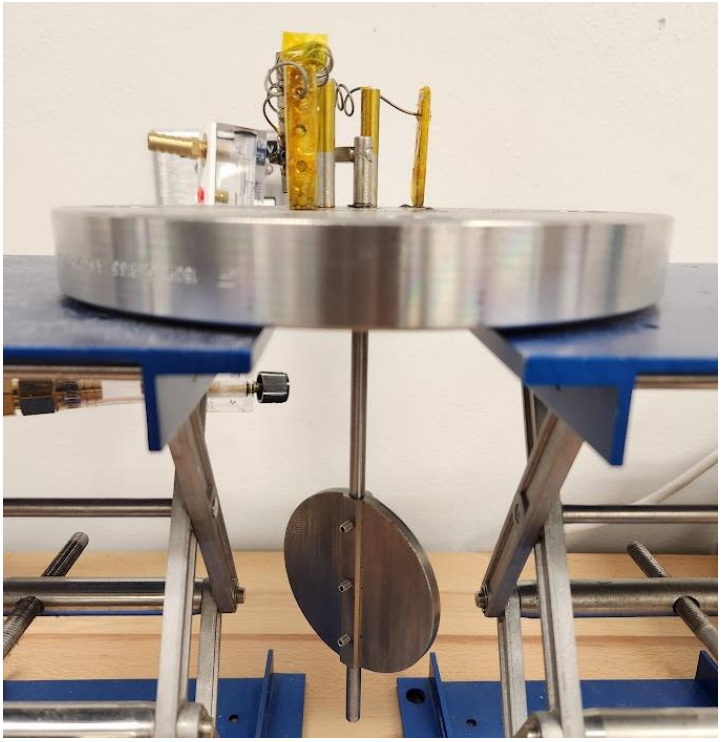

High-Temperature Stainless Steel Bypass Valve

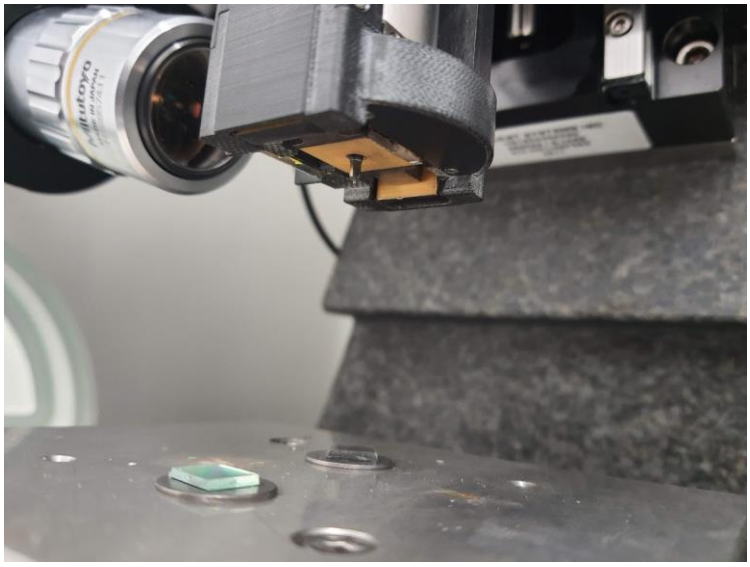

View of Berkovich Tip in Piezo Transducer Scanner

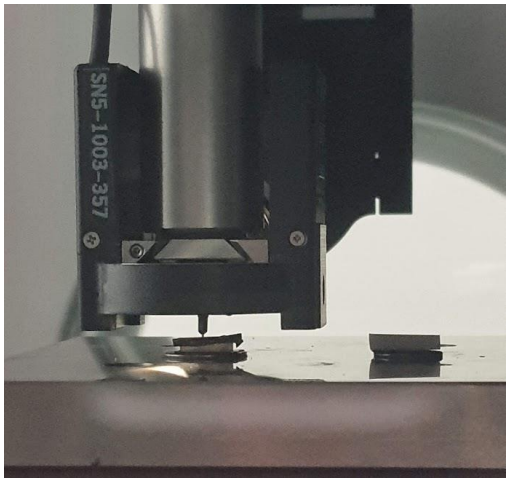

Close View During Indentation of a Sample

Appendix

NOMENCLATURE

τ	Shear Stress
γ	Strain
Ω	Phase Transformation Tensor
ξ	Degree of Martensitic Trans.
Θ	Thermoelastic Tensor
T	Temperature
K	Wahl Correction Factor
Ξ	
R	Mean Spring Radius
r	Radius of Spring Wire
G	Shear Modulus
α	Angular Deflection
N	Total Number of Coils
y	Total Deflection
μ	Poisson's Ratio
ṁ	Mass Flow Rate
F	External Force
P	Load
h	Distance
A	Area
Θ	Semi Angle

α	Effective Cone Angle
β	Geometry Correction Factor
H	Hardness
P_{max}	Max. Applied Load
h_f	Contact Indentation Depth
ε	Geometric Constant
S	Contact Stiffness
E_r	Elastic Modulus
E_s	Specimen Elastic Modulus
E_i	Indenter Elastic Modulus
v_s	Specimen Poisson's Ratio
v_i	Indenter Poisson's Ratio

Vita

Alba Jazmin Leyva Marquez received her Bachelor of Science from the University of Texas at El Paso in 2017. She also received her Master in Science from the University of Texas at El Paso in 2021. While attending the University of Texas at El Paso she conducted research for the Aerospace Center and worked as a teaching assistant for the department of Aerospace and Mechanical Engineering. During her time as a research assistant, she also held the position of Laboratory Manager for her research group.